

Identifying mantle carbonatite metasomatism through Os–Sr–Mg isotopes in Tibetan ultrapotassic rocks

Dong Liu^a, Zhidan Zhao^{a, *}, Di-Cheng Zhu^a, Yaoling Niu^{a, b}, Elisabeth Widom^c, Fang-Zhen Teng^d, Donald J. DePaolo^e, Shan Ke^{a, *}, Ji-Feng Xu^f, Qing Wang^a, Xuanxue Mo^a

- a. State Key Laboratory of Geological Processes and Mineral Resources, and School of Earth Science and Resources, China University of Geosciences, Beijing 100083, China
- b. Department of Earth Sciences, Durham University, Durham DH1 3LE, UK
- c. Department of Geology and Environmental Earth Science, Miami University, Oxford OH 45056, USA
- d. Department of Earth and Space Sciences, University of Washington, Seattle, WA 98195, USA
- e. Department of Earth and Planetary Science, University of California, Berkeley, CA 94720, USA
- f. State Key Laboratory of Isotope Geochemistry, Guangzhou Institute of Geochemistry, Chinese Academy of Sciences, Guangzhou 510640, China

Abstract: 217 words

Manuscript: 6411 words

Figure + Table: 8

Revised manuscript submitted to [EPSL](#)

***Corresponding authors:**

School of Earth Science and Resources, China University of Geosciences, 29 Xueyuan Road, Haidian District, Beijing 100083, China. Tel: (+86-10) 136-8111-8299; Fax: (+86-10) 8232-1115.

E-mail: zdzhao@cugb.edu.cn (Z. Zhao), keshan@cugb.edu.cn (S. Ke).

1 **Abstract**

2 Mantle-derived magmas at convergent plate boundaries provide unique insights into the
3 nature of materials subducted to and recycled from depths. Here we present a study of
4 Os–Sr–Mg isotopes on the Oligocene-Miocene ultrapotassic rocks aimed at better
5 understanding **sediment subduction and recycling** beneath southern Tibet. **New** isotopic data
6 confirm that ultrapotassic rocks in southern Tibet are of mantle origin, but underwent crustal
7 contamination as evidenced by **the** variably high $^{187}\text{Os}/^{188}\text{Os}$ that obviously deviates from
8 normal mantle reservoir. Still some samples with mantle-like $^{187}\text{Os}/^{188}\text{Os}$ exhibit $\delta^{26}\text{Mg}$
9 **significantly** lower than mantle and crustal lithologies, suggesting that **the isotopically light Mg**
10 **may not result from** crustal contamination but retain specific fingerprint of carbonate-related
11 metasomatism in mantle sources. Mantle carbonatite metasomatism is manifested by the
12 inverse $\delta^{26}\text{Mg}$ – $^{87}\text{Sr}/^{86}\text{Sr}$ correlations, as well as the depletion of high field strength elements
13 **relative to rare earth elements** and the enrichment of CaO in ultrapotassic rocks. The positive
14 co-variations between $\delta^{26}\text{Mg}$ and Hf/Sm defined by those low- $^{187}\text{Os}/^{188}\text{Os}$ ultrapotassic rocks
15 **provide evidence for** the potential of recycled dolomites to modify mantle Mg isotopic
16 composition. The correlated spatial variations of $\delta^{26}\text{Mg}$ and Hf/Sm **are interpreted to reflect**
17 **carbonatitic metasomatism associated with the northward subduction of the Neo-Tethyan**
18 **oceanic slab and its profound influence on postcollisional ultrapotassic magmatism.**

19 **Keywords:** Os–Sr–Mg isotopes; carbonatite metasomatism; ultrapotassic rocks; Neo-Tethyan
20 Ocean; Tibetan plateau

21 **1. Introduction**

22 Subduction of carbonate-bearing sediments at convergent plate boundaries has played a
23 fundamental role in mantle refertilization (White and Patchett, 1984; Plank and Langmuir, 1998;
24 Ducea et al., 2005) and in global carbon cycling (Connolly, 2005; Dasgupta and Hirschmann,
25 2010; Yang et al., 2012; Huang et al., 2015). Recently, volatile-rich mafic rocks including
26 kimberlite, carbonatite, and potassic rocks of mantle origin (e.g. kamafugite and ultrapotassic
27 rocks) have received an increasing amount of attention because of their petrogenetic links with
28 carbonate-related metasomatism in deep earth (Thomsen et al., 2008; Avanzinelli et al., 2009;
29 Liu et al., 2014a; Conticelli et al., 2015). Given the subduction of carbonate-rich Tethyan
30 seafloor (cf. Johnston et al., 2011), the widespread mantle-derived ultrapotassic rocks in the
31 Alpine-Himalaya orogenic belt thus offer a prime opportunity to investigate carbonatitic
32 metasomatism and carbon recycling processes in subduction zone.

33 In southern Tibet, however, carbonatite metasomatism associated with the Neo-Tethyan
34 seafloor subduction has long been understated (cf. Turner et al., 1996; Chung et al., 2005; Liu et
35 al., 2014a), which will inhibit us to better understand the geochemical evolution of lithospheric
36 mantle. Additionally, the inevitable crustal contamination, which has been amplified by crustal
37 thickening in response to the India-Asia convergence (cf. Liu et al., 2014b), constitutes another
38 difficulty in using mantle-derived rocks to probe the nature of mantle lithosphere. Selecting
39 process-sensitive tracer is therefore essential to ascertain the nature and extent of recycled
40 seafloor materials with respect to crustal contamination.

41 Because Os behaves much more compatible than its radioactive parent element Re during
42 mantle melting (Shirey and Walker, 1998), the residual mantle is strongly depleted in Re and

43 exhibits Os concentration much higher than those of metasomatic components, which makes
44 Re-Os isotopic system in mantle lithosphere essentially unaffected by subsequent metasomatic
45 modification (Schaefer et al., 2000; Meisel et al., 2001). On the other hand, Os isotopic
46 compositions of mantle-derived magmas are proved to be highly susceptible to crustal
47 contamination due to low Os concentrations (Shirey and Walker, 1998; Schaefer et al., 2000),
48 suggesting that Os isotopes in mantle-derived rocks can be utilized as a sensitive indicator for
49 crustal contamination. Meanwhile, higher MgO contents in ultrapotassic rocks relative to
50 crustal contaminants and limited Mg isotopic fractionation during high-temperature magmatic
51 processes (Teng et al., 2010) enable Mg isotopic tracer to preserve signatures of mantle sources.
52 The distinct Sr and Mg isotopic compositions between marine carbonates (Fantle and Higgins,
53 2014; Blättler et al., 2015) and terrestrial mantle reservoir (Teng et al., 2010) further indicate
54 the potential of these isotopic proxies for mantle carbonatite metasomatism (Yang et al., 2012;
55 Huang et al., 2015).

56 Here we present a systematic study on the Os, Sr, and Mg isotopes of the Tibetan
57 ultrapotassic rocks. The combined application of multiple isotopes and trace element allow us
58 to reveal the close relationship between the ultrapotassic rocks and mantle carbonatite
59 metasomatism, and to better understand mantle refertilization processes during the northward
60 subduction of Neo-Tethyan seafloor. As a case study, it also underscores the efficacy of Mg
61 isotopes in mantle-derived rocks to provide information about carbon recycling in deep earth.

62

63 **2. Geological setting**

64 As a micro-continent rifted away from the eastern margin of Gondwana (cf. Yin and
65 Harrison, 2000; Zhu et al., 2013), the Lhasa terrane in southern Tibet underwent a series of
66 seafloor subduction episodes that have modified its mantle lithosphere (cf. Kapp et al., 2007; Ji
67 et al., 2009; Zhu et al., 2013). As the northern boundary, the Bangong-Nujiang suture zone
68 (BNS) separates Lhasa terrane from Qiangtang terrane (Fig. 1). To the south, the Indus-Yarlung
69 Zangbo suture zone (IYZS) is viewed as remnants of the Neo-Tethyan seafloor lithologies
70 between Lhasa terrane and India plate (cf. Yin and Harrison, 2000; Zhu et al., 2013). Recent
71 studies reveal that the Lhasa terrane is composed of a reworked ancient crust in the center and
72 juvenile additions to its northern and southern edges (cf. Ji et al., 2009; Zhu et al., 2013).
73 Accordingly, the Lhasa terrane can be subdivided into the northern, central, and southern Lhasa
74 subterrane, which are separated by the Shiquan river-Nam Tso Mélange zone (SNMZ) and
75 Luobadui-Milashan fault (LMF) from north to south (Fig. 1a).

76 As products of the Tethyan seafloor subduction and the India-Asia continental collision
77 thereafter, the Mesozoic-early Cenozoic magmatic rocks are distributed roughly parallel to the
78 E–W trending Lhasa terrane (Fig. 1b). The Cretaceous volcanic rocks (131–91 Ma, Zhu et al.,
79 2013) are widespread in the northern and central Lhasa subterrane. The southern Lhasa
80 subterrane is dominated by the early Paleogene Linzizong volcanic sequence (69–43 Ma, Lee et
81 al., 2009), some of which extending into the eastern part of the central Lhasa subterrane (Fig.
82 1a). The Gangdese plutons outcrop widely in the Lhasa terrane and can be roughly divided into
83 the south Gangdese batholith (205–41 Ma, Ji et al., 2009; Zhu et al., 2013) associated with the
84 IYZS and the north Gangdese batholith (194–110 Ma, Zhu et al., 2013) distributing along the
85 BNS (Fig. 1a). With respect to the temporal and spatial distribution, the Mesozoic-early

86 Cenozoic magmatism in the Lhasa terrane has been interpreted as reflecting continued
87 Neo-Tethyan seafloor subduction, including low-angle northward subduction of the
88 Indus-Yarlung Zangbo Neo-Tethyan seafloor, slab rollback and subsequent break-off (cf. [Kapp
89 et al., 2007](#); [Ji et al., 2009](#)). Another attractive explanation is the bi-direction seafloor
90 subduction model (cf. [Zhu et al., 2013](#)), which is represented by southward subduction of the
91 Bangong-Nujiang Neo-Tethyan seafloor and northward subduction of the Indus-Yarlung
92 Zangbo Neo-Tethyan seafloor.

93

94 **3. Ultrapotassic volcanism and sample description**

95 Following the early-Paleogene India-Asia continental collision ([Yin and Harrison, 2000](#);
96 [Lee et al., 2009](#)), postcollisional magmatism in southern Tibet occurred in response to the
97 continued India-Asia convergence ([Turner et al., 1996](#); [Chung et al., 2005](#)). Mantle-derived
98 ultrapotassic volcanic rocks (UPVR) commonly occurred as lava flows in the central and
99 southern Lhasa subterranean ([Fig. 1a](#)), forming a magmatic belt with eruptive ages varying from
100 24 Ma to 10 Ma ([Liu et al., 2014b](#)). The mantle origin of the UPVR is indicated by mantle
101 xenoliths ([Liu et al., 2014c](#)), whereas the entrained crustal xenoliths of varying size (e.g. gabbro
102 and granite) also point to the significance of crustal contamination in petrogenesis of the UPVR
103 ([Liu et al., 2014b](#)). As ultrapotassic magmatism in southern Tibet is nearly coeval with the
104 accelerated plateau uplift and the east-west extension (cf. [Yin and Harrison, 2000](#); [Liu et al.,
105 2014a](#)), geodynamic models, such as convective thinning of mantle lithosphere ([Turner et al.,
106 1996](#)), removal or delamination of overthickened lithosphere ([Chung et al., 2005](#); [Zhao et al.,](#)

107 2009), and roll-back and break-off of the subducted Indian plate (Guo et al., 2013), have been
108 invoked to account for the mantle melting events during postcollisional stage.

109 We have collected a total of forty-seven UPVR samples with good spatial coverage of
110 ultrapotassic magmatism across the Lhasa terrane (Fig. 1a). Two crustal xenolith samples from
111 the host UPVR samples are also included in this study (Table 1). From basaltic trachyandesite
112 to trachyte, this suite of UPVR exhibits a wide lithological range with phenocrysts composed of
113 phlogopite, plagioclase, pyroxene, and minor olivine (Turner et al., 1996; Zhao et al., 2009).
114 The compositional and mineralogical ranges of the studied UPVR are comparable to the full
115 range of ultrapotassic rocks in southern Tibet (cf. review by Chung et al., 2005). High-quality
116 zircon U–Pb age data for these UPVR samples have been reported (cf. Liu et al., 2014b),
117 yielding the Oligocene–Miocene eruptive ages (24–10 Ma) agreeing within error with K–Ar
118 and Ar–Ar age data (Chung et al., 2005; Zhao et al., 2009). Sample details are listed in
119 supplementary Table S1.

120

121 4. Analytical methods

122 In order to minimize the influence of chemical weathering on isotopic composition,
123 weathered rock surfaces have been removed and thoroughly cleaned before analysis. After
124 extracting crustal and mantle xenoliths by handpicking, fresh samples (the chemical index of
125 alteration ranges from 27.6 to 51.0, Table S2) were powdered into 200 mesh. Major and trace
126 element compositions are reported in Table S2. Analytical results of Re–Os, Sr, and Mg
127 isotopes are given in Table 1.

128

129 **4.1. Major and trace element compositions**

130 Major and trace element analyses were conducted in the State Key Laboratory of
131 Geological Processes and Mineral Resources (GPMR), China University of Geosciences,
132 Wuhan. Rock powder (~0.5 g) was mixed with 5.0 g compound flux ($\text{Li}_2\text{B}_4\text{O}_7 : \text{LiBO}_2 = 12 : 22$)
133 and fused in a Pt-Au crucible by heating at ~1050°C for 11 minutes. The mixture was swirled
134 repeatedly to ensure complete molten and homogenization before pouring into a mould to form
135 a flat disc for analysis. Major elements were analyzed using a *Shimadzu XRF-1800* sequential
136 X-ray fluorescence spectrometry. The precision and accuracy for major element analysis are
137 better than 4% and 3%, respectively.

138 For trace element analysis, the rock powder (~50 mg) was dissolved in a Teflon bomb with
139 HF + HNO₃ mixture and then was heated at 190°C for 48 h. After evaporating the solution to
140 dryness, the dried sample was re-dissolved using ~3 ml of 30% HNO₃, and then heated at
141 190°C for 24 h. The final solution was diluted to ~100 g with 2% HNO₃ for subsequent analysis.
142 Trace elements were analyzed using an *Agilent 7500a* inductively coupled plasma-mass
143 spectrometry (ICP-MS). Analytical results of procedural blanks and international rock
144 standards are given in [Table S3](#).

145

146 **4.2. Rhenium–osmium and strontium isotopic compositions**

147 Re and Os isotopic analyses were conducted at the Guangzhou Institute of Geochemistry,
148 Chinese Academy of Sciences (GIG-CAS), with some samples analyzed at the Miami
149 University (Miami U.). In GIG-CAS, rock powders (~2 g), spiked with ¹⁸⁵Re and ¹⁹⁰Os, were
150 frozen with inverse aqua regia into Carius tubes before being sealed and heated at 240°C for 24

151 h. The separation of Re and Os was performed using a carbon tetrachloride aqua (CCl₄) solvent
152 extraction method and Os was further purified by microdistillation. Purified Os was loaded
153 using Ba(NO₃)₂ as emission enhancer on Pt filaments and determined using *Finnigan Triton*
154 thermal ionization mass spectrometer (TIMS) operated in the negative ion mode. Re was
155 separated and purified from the liquid remaining after extraction of Os using AG50W-X8 (200
156 – 400 mesh) cation exchange columns and BPHA (100 mesh) extraction chromatographic
157 columns. Isotope dilution analysis of Re was conducted on a *Thermo-Scientific X series-2*
158 ICP-MS. Instrumental mass fractionation of Os was corrected by normalizing the measured
159 ¹⁹²Os/¹⁸⁸Os to 3.08271. Analytical uncertainty for Os concentration and ¹⁸⁷Os/¹⁸⁸Os are less
160 than 0.5 % within two times of the standard deviation (2σ). Total procedural blanks for Re and
161 Os were ~20 pg and 0.18 pg, respectively, yielding average ¹⁸⁷Os/¹⁸⁸Os of 0.350 (Table S4).
162 The contribution of the blank to measured Os concentration and ¹⁸⁷Os/¹⁸⁸Os were < 3% and <
163 10%, respectively.

164 In the Miami U., rock powders (~1 g) were spiked with ¹⁸⁵Re and ¹⁹⁰Os and digested with
165 concentrated inverse aqua regia in sealed Carius tubes by heating at 230°C for 48 h. The
166 separation of Re and Os was performed using a CCl₄ solvent extraction method, and Os was
167 further purified by microdistillation. Re was separated and purified from the liquid remaining
168 after extraction of Os using AG1-X8 anion exchange columns. Purified Os was loaded on Pt
169 filaments along with Ba(OH)₂ as emission enhancer, and Os isotope ratio was determined using
170 negative TIMS as OsO₃⁻ using *Finnigan Triton* TIMS. Os isotope ratios were corrected for
171 mass fractionation using ¹⁹²Os/¹⁸⁸Os = 3.0826. Re concentrations were measured by isotope

172 dilution by negative TIMS as ReO_4^- . Total procedural blanks were ~ 2 pg for Re and ~ 0.1 pg for
173 Os. The average $^{187}\text{Os}/^{188}\text{Os}$ of unspiked blanks was 0.184 (Table S4).

174 The Sr isotopic analyses were carried out on a *Micromass ISOPROBE* MC-ICP-MS at
175 GIG-CAS. Rock powders (50 – 100 mg) were dissolved in screw-top PFA beakers using a 1:2
176 (v/v) mixture of HNO_3 and HF acids. The capped beakers were heated at 140°C for 7 days
177 before opened and then evaporated to dryness. The separation of Sr was done using cation
178 exchange columns. All the measured Sr isotopic ratios were corrected for mass fractionation
179 using $^{86}\text{Sr}/^{88}\text{Sr} = 0.1194$. Multiple analyses of the BHVO-2 and NBS-987 yield average
180 $^{87}\text{Sr}/^{86}\text{Sr}$ of 0.703469 ± 0.000010 (2σ , $n = 2$) and 0.710268 ± 0.000010 (2σ , $n = 7$), respectively
181 (Table S5).

182

183 4.3. Magnesium isotope compositions

184 The Mg isotopic analyses, using the sample-standard bracketing method, were conducted
185 using a *Nu Plasma* HR MC-ICP-MS at the Isotope Laboratory of the University of Arkansas
186 and using a *Neptune plus* MC-ICP-MS at the China University of Geosciences, Beijing,
187 respectively. Rock powders (1 – 20 mg) were dissolved in screw-top beakers using a 3:1 (v/v)
188 mixture of Optima-grade HF and HNO_3 acids. These capped beakers were heated at $70 - 80^\circ\text{C}$,
189 and then the solutions were evaporated to dryness. The dried samples were refluxed with a 3:1
190 (v/v) mixture of HCl and HNO_3 , and then evaporated again to achieve 100% dissolution. The
191 residues were then dissolved in 1N HNO_3 for chromatographic separation. Separation of Mg
192 was achieved using cation exchange columns loaded with 1 ml pre-cleaned resin (BioRad 200 –
193 400 mesh AG50W-X8), with 1N HNO_3 used as leaching agent (Teng et al., 2010). The Mg

194 yields range from 99.5% to 99.9%. Samples were passed through the columns twice to achieve
195 the required level of purification. Total procedural blank for Mg was < 15 ng. The analytical
196 results for magnesium isotopes are expressed as δ -notation in per mil relative to DSM3: $\delta^X\text{Mg} =$
197 $[(^X\text{Mg}/^{24}\text{Mg})_{\text{sample}} / (^X\text{Mg}/^{24}\text{Mg})_{\text{DSM3}} - 1] \times 1000$, where X refers to mass 25 or 26 and DSM3 is
198 a magnesium solution made from pure Mg metal (Galy et al., 2003). The analyses of AGV-2,
199 BCR-2, BHVO-2, Kilbourne Hole olivine, and Hawaii seawater yield weighted average $\delta^{26}\text{Mg}$
200 values in good agreement with recommended values within 2σ error (Table S6).

201

202 5. Results

203 The UPVR samples have broad ranges of SiO_2 (45.4 – 60.6 wt.%), MgO (2.9 – 12.3 wt.%),
204 CaO (1.9 – 10.1 wt.%), and K_2O (5.0 – 8.3 wt.%) (Table S2). Most UPVR samples are basaltic
205 trachyandesite and trachyandesite, with a few samples plotted in the fields of tephrite (GGP-7),
206 tephriphonolite (XR02-1), and trachyte (DR01-2, 10XB15, and XB1232) (Fig. 2a). Both
207 gabbroic ($\text{SiO}_2 = 50.1$ wt.%) and granitic ($\text{SiO}_2 = 69.7$ wt.%) xenoliths have been identified
208 from ultrapotassic rocks (Fig. 2a). In the primitive mantle-normalized incompatible trace
209 element diagram (Fig. 2b), a remarkable feature of the UPVR is the depletion of high field
210 strength elements (HFSEs, e.g., Nb, Ta and Ti) relative to rare earth elements (REEs). Negative
211 anomalies in Zr and Hf can be found in the UPVR (Fig. 2b), and Hf/Sm ratio decreases with
212 increasing $\text{Mg}^\#$ and $\text{CaO}/\text{Al}_2\text{O}_3$ (Figs. 2c and 2d). Unlike the UPVR, Zr and Hf anomalies are
213 rather weak for gabbroic and granitic xenoliths (Fig. 2b).

214 The UPVR samples display wide ranges of Re (0.004 – 0.416 ppb) and Os (0.004 – 0.698
215 ppb), and have more radiogenic Os isotopic compositions ($^{187}\text{Os}/^{188}\text{Os} = 0.1315 - 0.7197$,

216 **Table 1**) than the primitive upper mantle ($^{187}\text{Os}/^{188}\text{Os} = 0.1296$, Meisel et al., 2001) and the
217 entrained peridotite xenoliths ($^{187}\text{Os}/^{188}\text{Os} = 0.1246$, **Table S7**). Os concentration and
218 $^{187}\text{Os}/^{188}\text{Os}$ ratio in gabbroic xenolith are 0.034 ppb and 0.2249, respectively. In the plot of
219 $^{187}\text{Os}/^{188}\text{Os}$ vs. $1/\text{Os}$ (**Fig. 3a**), a scattered but positive correlation can be observed in the
220 samples. The Tibetan UPVR samples also exhibit extremely radiogenic Sr isotopic
221 compositions ($^{87}\text{Sr}/^{86}\text{Sr} = 0.710747 - 0.736451$, **Table 1**) as discussed previously (Chung et
222 2005; Zhao et al., 2009). The relatively low $^{87}\text{Sr}/^{86}\text{Sr}$ in gabbroic (0.709763 ± 0.000013) and
223 granitic xenoliths (0.713443 ± 0.000011) are distinguishable from the host UPVR samples.

224 Compared with mantle peridotite ($\delta^{26}\text{Mg} = -0.25 \pm 0.04\text{‰}$, Teng et al., 2010), the $\delta^{26}\text{Mg}$
225 values of mantle-derived ultrapotassic rocks are more variable (-0.22 to -0.46‰ , **Table 1**).
226 Heavy Mg isotopic composition shown by gabbroic xenolith ($\delta^{26}\text{Mg} = -0.12 \pm 0.06\text{‰}$) is
227 comparable with that of lower continental crust (average $\delta^{26}\text{Mg} = -0.19\text{‰}$, Teng et al., 2013).
228 In contrast, granitic xenolith has a light Mg isotopic composition, with $\delta^{26}\text{Mg}$ as low as -0.49
229 $\pm 0.05\text{‰}$ (**Table 1**). In the plot of $\delta^{25}\text{Mg}$ vs. $\delta^{26}\text{Mg}$ (**Fig. 3b**), the measured Mg isotopes follow
230 the terrestrial mass-dependent equilibrium fractionation trend with a slope close to 0.521.
231 According to the $\delta^{26}\text{Mg}-^{187}\text{Os}/^{188}\text{Os}$ correlation (**Fig. 3c**), two kinds of UPVR samples can be
232 identified: (i) samples with varying $^{187}\text{Os}/^{188}\text{Os}$ and mantle-like $\delta^{26}\text{Mg}$ (trend A), and (ii)
233 samples showing restricted $^{187}\text{Os}/^{188}\text{Os}$ but variably lower $\delta^{26}\text{Mg}$ (trend B).

234

235 **6. Discussion**

236 **6.1. Crustal contamination effects on isotopic compositions of ultrapotassic rocks**

237 Tibetan ultrapotassic rocks have long been treated as primitive melts of mantle peridotite
238 (e.g. Zhao et al., 2009; Guo et al., 2013) due to the entrainment of mantle xenoliths (Liu et al.,
239 2014c) and high Mg[#] (up to 76) and compatible element (e.g. Cr, Co, Ni) concentrations.
240 However, caution is required in using isotope data of mantle-derived rocks to infer the nature
241 of subcontinental lithospheric mantle (SCLM) because of the likely crustal
242 contamination/assimilation in orogenic belts (Schaefer et al., 2000; Liu et al., 2014a). In
243 southern Tibet, entrained crustal fragments and zircon xenocrysts of crustal origin indicate
244 that both upper and lower crustal materials of the Lhasa terrane have been incorporated into
245 ultrapotassic magma (Liu et al., 2014b). For this reason, the effects of crustal contamination
246 on isotopic compositions of ultrapotassic rocks should be assessed before using these proxies
247 to reveal mantle geochemical evolution beneath southern Tibet.

248

249 **6.1.1. The susceptibility of Os isotopes to crustal contamination**

250 During crust-mantle segregation and mantle partial melting, Re behaves as a moderately
251 incompatible element while Os is strongly compatible (Shirey and Walker, 1998), which
252 results in high Os concentration and uniform ¹⁸⁷Os/¹⁸⁸Os in residual mantle (Meisel et al.,
253 2001). Such partitioning behaviors also lead to high Re/Os in continental crust that
254 consequently develop variably high ¹⁸⁷Os/¹⁸⁸Os through radiogenic ingrowth of ¹⁸⁷Os from
255 the β-decay of ¹⁸⁷Re (Saal et al., 1998; Peucker-Ehrenbrink and Jahn, 2001). The upper
256 continental crust is characterized by low Os concentration and extremely high ¹⁸⁷Os/¹⁸⁸Os (e.g.
257 Os = 0.031 ppb, ¹⁸⁷Os/¹⁸⁸Os = 1.4 ± 0.3, Peucker-Ehrenbrink and Jahn, 2001). Compared with
258 upper continental crust, the lower continental crust has higher Os concentration and less

259 radiogenic Os isotopic composition (e.g. Os = 0.109 ppb, $^{187}\text{Os}/^{188}\text{Os} = 0.795$, Saal et al.,
260 1998). Because the Lhasa terrane has undergone episodes of juvenile crust formation in the
261 Mesozoic-Cenozoic (cf. Ji et al., 2009; Zhu et al., 2013), the Os isotopic composition of lower
262 crust would be more heterogeneous and unradiogenic because the juvenile crust additions (e.g.
263 gabbroic xenoliths, sample XB1260) commonly yield low $^{187}\text{Os}/^{188}\text{Os}$ as a result of short crust
264 formation age and limited radiogenic ingrowth of ^{187}Os .

265 As illustrated in Fig. 3a, simple magma-mixing process cannot account for the UPVR
266 samples with high $^{187}\text{Os}/^{188}\text{Os}$ unless a large amount of crustal materials are incorporated into
267 primitive ultrapotassic magma. Together with the convex upward $\delta^{18}\text{O}-^{87}\text{Sr}/^{86}\text{Sr}$ correlations
268 (i.e. the crustal contamination trend defined by O and Sr isotopes, Liu et al., 2014a), the
269 presence of crustal xenoliths and zircon xenocrysts in the UPVR (Liu et al., 2014b)
270 demonstrates the occurrence of crustal assimilation during magmatic evolution. Furthermore,
271 the fractional crystallization of olivine and sulfide will dramatically decrease Os
272 concentrations of remaining magmas (Saal et al., 1998), and result in their Re–Os isotope
273 system being extremely susceptible to crustal contamination. Based on aforementioned Os
274 isotopic signatures of continental crust, we modeled the assimilation and fractional
275 crystallization (AFC) processes and found that AFC modeling can fully reproduce Os isotopic
276 variation observed in the Tibetan ultrapotassic rocks (Fig. 3a). For the UPVR samples with
277 high $^{187}\text{Os}/^{188}\text{Os}$ (> 0.3), their radiogenic Os isotopic compositions may document the
278 extensive crustal contamination with large amounts of high- $^{187}\text{Os}/^{188}\text{Os}$ crustal materials (e.g.
279 upper crust and lower crust with sedimentary origin) incorporated into ultrapotassic magma
280 (Fig. 3a). The UPVR samples with $^{187}\text{Os}/^{188}\text{Os}$ slightly deviated from the mantle value reflect

281 magmas undergoing low-level crustal contamination and assimilating crustal materials
282 showing $^{187}\text{Os}/^{188}\text{Os}$ as low as the entrained gabbroic xenolith (Fig. 3a). Therefore,
283 considering the Oligocene-Miocene age of ultrapotassic magmatism (24 – 10 Ma, Liu et al.,
284 2014b), the radiogenic Os isotopic compositions in the UPVR corroborate the role of crustal
285 contamination/assimilation in petrogenesis of the Tibetan ultrapotassic rocks.

286

287 6.1.2. Limited effects of crustal contamination on Mg isotopes of the UPVR

288 But, unlike the Re-Os isotopic system, crustal contamination cannot fully account for the
289 overall light Mg isotopic signatures in the Tibetan ultrapotassic rocks (Fig. 3c), especially for
290 the low- $^{187}\text{Os}/^{188}\text{Os}$ UPVR samples that exhibit light Mg isotopic compositions (trend B in
291 Fig. 3c). Recent studies reveal that light Mg isotope is prone to partition into liquid during
292 chemical weathering and heavy Mg isotope will be left in the residue (cf. Li et al., 2010). Due
293 to the influence of surface weathering, the average Mg isotopic compositions of upper ($\delta^{26}\text{Mg}$
294 = -0.22‰ , Li et al., 2010) and lower continental crust ($\delta^{26}\text{Mg}$ = -0.18‰ , Teng et al., 2013)
295 are proved to be slightly heavier than mantle peridotites ($\delta^{26}\text{Mg}$ = $-0.25 \pm 0.04\text{‰}$) and basalts
296 (MORB: $\delta^{26}\text{Mg}$ = $-0.25 \pm 0.06\text{‰}$; OIB: $\delta^{26}\text{Mg}$ = $-0.26 \pm 0.08\text{‰}$) (Teng et al., 2010). In this
297 case, assimilating continental crust components like the entrained gabbroic xenolith ($\delta^{26}\text{Mg}$ =
298 $-0.12 \pm 0.06\text{‰}$, Table 1) would only make Mg isotopes of ultrapotassic magma heavier than
299 the mantle reservoir, contrasting with the overall light Mg isotopic compositions in the
300 Tibetan UPVR (Fig. 3b).

301 Even if the heterogeneity in Mg isotopic composition of continental crust is considered
302 (Li et al., 2010; Teng et al., 2013), higher MgO contents in mantle-derived ultrapotassic rocks

303 than crustal contaminants further indicate that there is little leverage to change Mg isotopic
304 compositions of ultrapotassic magmas through low-level crustal contamination. This
305 suggestion is supported by the mantle-like Mg isotopic composition shown by the host UPVR
306 sample (MgO = 8.09 wt.%, $\delta^{26}\text{Mg} = -0.29 \pm 0.04\text{‰}$) of granitic xenolith (MgO = 0.61 wt.%,
307 $\delta^{26}\text{Mg} = -0.49 \pm 0.05\text{‰}$) (Table 1). Additionally, the correlations between Os and Mg
308 isotopes provide evidence for the limited role of crustal contamination in changing Mg
309 isotopic compositions of the UPVR (Fig. 3c). As predicted by AFC modeling (Fig. 3c),
310 crustal contamination gives rise to dramatic increases in $^{187}\text{Os}/^{188}\text{Os}$ of mantle-derived
311 ultrapotassic magmas (trend A in Fig. 3c). Meanwhile, substantial changes in $\delta^{26}\text{Mg}$ are not
312 observed until large amounts of low-MgO crustal materials, such as pelites (MgO = 3.55
313 wt.%; $\delta^{26}\text{Mg} = -0.52 \pm 0.07\text{‰}$, Li et al., 2010) and felsic granulite (MgO = 2.71 wt.%, $\delta^{26}\text{Mg}$
314 = $-0.72 \pm 0.08\text{‰}$, Teng et al., 2013), are incorporated into ultrapotassic magmas. The
315 contrasting effects of crustal contamination on Os and Mg isotopic variations can still be
316 observed in AFC modeling even if the MgO content of primitive magma is assumed to be as
317 low as 8 wt.%. We thus conclude that the overall light Mg isotopic signature, particularly for
318 the variably low $\delta^{26}\text{Mg}$ in those less contaminated UPVR samples (i.e. $^{87}\text{Os}/^{188}\text{Os} < 0.3$), may
319 not be result of low-level crustal contamination.

320

321 6.1.3. Contaminated by carbonate wall-rocks during magmatic ascent?

322 Unlike silicate crust components, sedimentary carbonate is an important low- $\delta^{26}\text{Mg}$
323 reservoir in the Earth (-5.28 to -1.09‰ , Young and Galy, 2004), which means that
324 incorporation of Mg-rich carbonates (i.e. dolostone) can shift $\delta^{26}\text{Mg}$ of the UPVR to lower

325 values. Moreover, previous works regarding the interaction between carbonate wall-rocks and
326 ultrapotassic magmas have shown that incorporation of carbonates during magmatic evolution
327 can lead to significant increases of bulk-rock $\delta^{18}\text{O}_{\text{V-SMOW}}$ (up to 13.3‰) and CaO content (up
328 to 23.05 wt.%, Peccerillo et al., 2010) (Fig. 4). Incorporation of carbonates into mafic rocks
329 would also lead to crystallization of CaO-rich mineral phases during magmatic evolution (e.g.
330 CaO content in olivine is up to 1.63 wt.%, Wenzel et al., 2002).

331 Notwithstanding, many lines of evidence preclude the interaction between sedimentary
332 carbonates and ultrapotassic magma as a controlling process to generate the Mg and O
333 isotopic signatures observed in the Tibetan UPVR. First, carbonate xenoliths or globules have
334 not been identified from the Tibetan ultrapotassic rocks so far (cf. Liu et al., 2014a), and
335 phenocrysts such as olivines in the UPVR are reported to have low CaO contents (< 0.25
336 wt.%, Turner et al., 1996; Zhao et al., 2009). In addition, the Tibetan UPVR samples display
337 poorly varying and lower CaO/SiO₂ (< 0.2, Fig. 4a), which apparently differs from the Alban
338 Hills ultrapotassic rocks that underwent carbonate contamination (Peccerillo et al., 2010).
339 Another argument against carbonate contamination comes from the positive correlation
340 between $\delta^{18}\text{O}_{\text{V-SMOW}}$ and SiO₂ defined by the Tibetan UPVR (Fig. 4b), which imply that the
341 elevation of bulk-rock $\delta^{18}\text{O}_{\text{V-SMOW}}$ is due to the input of SiO₂-rich components rather than
342 carbonates contamination.

343 Collectively, AFC processes can reproduce Os isotopic variations in the Tibetan
344 ultrapotassic rocks but fail to fully recreate their Mg isotopic signatures. For the UPVR
345 samples with low $^{187}\text{Os}/^{188}\text{Os}$, their variably low $\delta^{26}\text{Mg}$ may be inherited from metasomatized
346 mantle sources rather than obtained through contamination by varying crustal lithologies.

347

348 **6.2. Geochemical fingerprints of mantle carbonatite metasomatism**

349 **6.2.1. Mantle metasomatism recorded in the entrained mantle xenoliths**

350 Metasomatized mantle sources are requisite for generating potassium-rich mafic rocks
351 with enriched isotopic compositions and extremely high concentrations of incompatible
352 elements (Foley et al., 1987). For ultrapotassic magmatism in circum-Tethyan realm, the
353 subduction of Tethyan seafloor has been invoked to supply oceanic sediments (i.e.,
354 terrigenous sediments and deep-sea carbonates) to refertilize mantle sources (e.g. Avanzinelli
355 et al., 2009; Conticelli et al., 2015). Similarly, lithospheric mantle beneath the Lhasa terrane
356 has been significantly metasomatized during the Tethyan seafloor subduction and the
357 underthrusting of Indian continental lithosphere thereafter (cf. Chung et al., 2005; Zhao et al.,
358 2009; Liu et al., 2014c).

359 Mineralogical and geochemical fingerprints preserved in mantle xenoliths provide
360 important constraints on the geochemical evolution of mantle lithosphere. Recently, a
361 high- $\delta^{18}\text{O}$ mantle region has been recognized beneath southern Tibet with the aid of in-situ
362 oxygen isotopic analyses on olivines separated from mantle xenoliths (Liu et al., 2014c).
363 Accordingly, the primitive UPVR samples, with high MgO contents (up to 12.5 wt.%) and
364 $\text{Mg}^\#$ values (up to 76), exhibit oxygen isotopic compositions ($\delta^{18}\text{O}_{\text{V-SMOW}} = 7.6 - 8.1\%$, Zhao
365 et al., 2009) that are comparable with this newly identified high- $\delta^{18}\text{O}$ mantle domain
366 ($\delta^{18}\text{O}_{\text{V-SMOW}}$ up to 8.03%, Liu et al., 2014c). Besides, the low Ti/Eu (< 1500) and high
367 (La/Yb)_N (up to 89.5) features shown by clinopyroxenes with low Al₂O₃ contents in mantle
368 xenoliths also suggest their origin of mantle carbonatite metasomatism (Coltorti et al., 1999)

369 (Fig. S1). Considering that carbonatite metasomatism will increase clinopyroxene abundances
370 in mantle assemblage at the expense of orthopyroxene (Coltorti et al., 1999; Huang et al.,
371 2011), a high- $\delta^{18}\text{O}$ metasomatic agent like recycled marine carbonate (e.g. $\delta^{18}\text{O}$ for calcites in
372 mantle peridotite is up to 20.5‰, Ducea et al., 2005) is necessary to modify mantle lithology
373 and oxygen isotopic composition beneath southern Tibet.

374

375 6.2.2. Identifying mantle carbonatite metasomatism through Os–Sr–Mg isotopes

376 With respect to the metasomatic fingerprints left in mantle xenoliths, the relevance of
377 carbonatite metasomatism and ultrapotassic magmatism in southern Tibet cannot be
378 understated. Besides, potassium-rich silicate melts observed in melting experiments of
379 carbonated pelite (850 – 1300 °C, 2.5 – 5.0 GPa, Thomsen and Schmidt, 2008) also indicate
380 the genetic links between carbonatite metasomatism and mantle-derived potassium-rich
381 magmatism as well. If we considered that Lhasa terrane had drifted across the Tethys ocean
382 during the Mesozoic (cf. Yin and Harrison, 2000, Zhu et al., 2013), the nature of subducted
383 marine sediments thus directly affects the manner in which we interpret the geochemical
384 signatures of the Tibetan ultrapotassic rocks. Previous works reveal that the Tethys ocean,
385 which opened around the equator, may have greater carbonate compensation depth and
386 accumulate more carbonates and organic-rich sediments due to the influence of equatorial
387 upwelling (cf. Johnston et al., 2011). Moreover, the microbial dolomite model highlights the
388 role of bacteria activity in overcoming kinetic barrier for dolomite nucleation at
389 low-temperature, and promoting the precipitation of dolomite within anoxic, organic-rich
390 deposits in deep-sea settings (cf. Mazzullo, 2000; Sánchez-Román et al., 2009; Blättler et al.,

391 2015). The Mesozoic carbonate turbidite sequences found in Tethys domain (e.g. Wang et al.,
392 2005) indicates that shelf carbonates can be transported into or beyond the trench by turbidity
393 current and finally involved in seafloor subduction (cf. Yang et al., 2012).

394 Combined with the extremely light Mg isotopic compositions in marine carbonates
395 (Fantle and Higgins, 2014; Blättler et al., 2015), we suggest that carbonate-rich Tethyan
396 sediments may have played a crucial role in replenishing mantle sources of the Tibetan
397 ultrapotassic rocks. This suggestion is supported by the low Hf/Sm and high CaO/Al₂O₃ ratios
398 in those primitive UPVR samples (Figs. 2c and 2d), because carbonatitic metasomatism will
399 increase CaO contents of mantle sources and make mantle assemblages strongly depleted in
400 HFSEs (i.e. low Hf/Sm) (Ducea et al., 2005; Huang et al., 2011). In addition, it is difficult for
401 recycled marine carbonates, with low Os concentrations (Ravizza, 1993), to change mantle Os
402 isotopic composition. Accordingly, carbonatitic metasomatism has potential to fully
403 reproduce the considerable variation of $\delta^{26}\text{Mg}$ in those less contaminated ultrapotassic rocks
404 (trend B in Fig. 3c). Recent study regarding Sr and Ca isotopes of Hawaiian shield lavas also
405 highlights the presence of subducted carbonates in mantle sources and their capacity of
406 raising $^{87}\text{Sr}/^{86}\text{Sr}$ in mantle lithology (Huang et al., 2011). Hence, mantle carbonatite
407 metasomatism occurred beneath southern Tibet can also be manifested by the negative
408 correlations between $\delta^{26}\text{Mg}$ and $^{7}\text{Sr}/^{86}\text{Sr}$ in the low- $^{187}\text{Os}/^{188}\text{Os}$ UPVR samples (Fig. 5a).

409 However, recycling marine carbonates into mantle sources cannot fully explain the
410 variably high $^{87}\text{Sr}/^{86}\text{Sr}$ in ultrapotassic rocks (Fig. 5a), as the $^{87}\text{Sr}/^{86}\text{Sr}$ of subducted carbonates
411 (≤ 0.71 , Fig. 5a) are not high enough to dramatically increase mantle Sr isotopic composition.
412 Even if pronounced increases of $^{87}\text{Sr}/^{86}\text{Sr}$ can be observed when voluminous crustal materials

413 were incorporated into ultrapotassic magma (> 10% AFC, Fig. 5a), low-¹⁸⁷Os/¹⁸⁸Os signatures
414 in these UPVR samples argue against extensive crustal contamination (Fig. 3a). Besides,
415 much higher Sr concentrations in ultrapotassic magmas (most > 1000 ppm, Table S2) relative
416 to crustal contaminants will only give rise to minor increases in ⁸⁷Sr/⁸⁶Sr during low-level
417 crustal contamination (shaded area in Fig. 5a). Given that subducting sediments are
418 overwhelmingly terrigenous (Plank and Langmuir, 1998), a considerable fraction of ⁸⁷Sr/⁸⁶Sr
419 in the Tibetan UPVR could be due to the subduction of terrigenous sediments (GLOSS:
420 ⁸⁷Sr/⁸⁶Sr = 0.717, Fig. 5a). In this scenario, the extremely radiogenic Sr isotopic compositions
421 can be reconciled with the joint contribution from mantle metasomatism and low-level crustal
422 contamination thereafter (cf. Liu et al., 2014a). It can be concluded that the variably lower
423 $\delta^{26}\text{Mg}$ values, as well as negative Mg–Sr isotopic correlations defined by those less
424 contaminated UPVR samples, provide evidence for the involvement of carbonate-bearing
425 sediments in mantle refertilization beneath southern Tibet.

426

427 **6.2.3. Implications for the effect of carbonatitic metasomatism on mantle Mg isotopic** 428 **composition**

429 Although both calcite and dolomite are reported to have low $\delta^{26}\text{Mg}$ values (Fantle and
430 Higgins, 2014; Blättler et al., 2015), much more low-Mg carbonates are needed to modify
431 mantle Mg isotopic composition (Figs. 3c and 5a). Besides, compared with dolomite-rich
432 carbonates, calcite-rich carbonates cannot remain stable at high-pressure condition (Dasgupta
433 and Hirschmann, 2010). Significant Mg isotopic exchanges between limestone and eclogitic
434 oceanic crust further imply that calcite cannot keep its low $\delta^{26}\text{Mg}$ signature during prograde

435 metamorphism (Wang et al., 2014). These findings cast doubts on the capacity of calcite-rich
436 carbonates to cause Mg isotopic heterogeneity in mantle lithosphere.

437 For these reasons, we need a geochemical proxy for carbonatitic metasomatism to clarify
438 which kind of marine carbonates can effectively change mantle Mg isotopic composition.
439 Compared with $^{87}\text{Sr}/^{86}\text{Sr}$ and CaO, Hf/Sm ratio in mantle-derived rocks may be more suitable
440 not only because carbonates are extremely depleted in Zr and Hf (Hf/Sm < 0.1, Fig. 2b), but
441 because Hf and Sm have similar incompatibility during mantle melting and fractional
442 crystallization (Sun and McDonough, 1989; Handley et al., 2011). The similar incompatibility
443 between Hf and Sm during magmatism suggests that they will not fractionate from each other.
444 Hence Hf/Sm variation in mantle-derived magmatic rocks can largely reflect the nature of
445 mantle sources without being affected by different degree of mantle partial melting. This is
446 consistent with the similar Hf/Sm ratios in ocean island basalts (Hf/Sm = 0.78) and mid-ocean
447 ridge basalts (Hf/Sm = 0.78, Sun and McDonough, 1989) (Fig. 5b). Additionally, the Hf/Sm
448 of continental crust (0.68 – 1.13, Rudnick and Gao, 2003) and global subducting sediments
449 (GLOSS, 0.70, Plank and Langmuir, 1998) are comparable with that of primitive mantle (0.70,
450 Sun and McDonough, 1989), ruling out the interference from terrigenous sediment subduction
451 and crustal contamination (Fig. 2b). Therefore, the combined use of $\delta^{26}\text{Mg}$ □ □ □ Hf/Sm will
452 allow us to better constrain mantle carbonatite metasomatism beneath southern Tibet.

453 Based on the intrinsic Mg isotopic variations in marine carbonates (Fantle and Higgins,
454 2014; Blättler et al., 2015) and their trace element variations during prograde metamorphism
455 (Li et al., 2014), we modeled carbonatitic metasomatism in terms of binary mixing between
456 mantle lherzolite and recycled carbonates with various Mg/Ca (Fig. 5b). It can be found that,

457 with marine carbonates involved in the metasomatism, mantle peridotite becomes depleted in
458 HFSEs and has lighter Mg isotopic composition (Fig. 5b). The poorly varying $\delta^{26}\text{Mg}$ indicate
459 that recycled calcites cannot effectively change mantle Mg isotopic composition because their
460 MgO contents are much lower than that of peridotite (Fig. 5b). Meanwhile, extensive isotopic
461 exchanges with underlying eclogite during prograde metamorphism will even give rise to
462 heavier Mg isotopes in calcite-rich carbonates (Wang et al., 2014), which makes it more
463 difficult for recycled calcites to modify mantle Mg isotopic composition.

464 Conversely, subducted dolomites, with high MgO contents, are capable of preserving their
465 initially light Mg isotopic compositions during prograde metamorphism (Wang et al., 2014),
466 and thus have potential to leave Mg isotopic fingerprints in mantle lithosphere. As modeled in
467 Fig. 5b, the $\delta^{26}\text{Mg}$ –Hf/Sm correlations in the Tibetan UPVR match well with the binary
468 mixing trends defined by mantle lherzolite and recycled dolomites with Mg/Ca ranging from
469 1.04 to 0.60. Apart from the Tibetan ultrapotassic rocks, the potential of recycled dolomites to
470 modify mantle Mg isotopic compositions is further revealed by $\delta^{26}\text{Mg}$ –Hf/Sm correlations in
471 kamafugites from western Qinling orogenic belt, the Cretaceous basalts from north China
472 craton (ca. 100 Ma, Yang et al., 2012), and the Cenozoic basalts from south China (13–3 Ma,
473 Huang et al., 2015) (Fig. 5b). It seems that the co-variations between $\delta^{26}\text{Mg}$ □ □ □ □ Hf/Sm
474 in the UPVR not only provide strong argument for mantle carbonatite metasomatism beneath
475 southern Tibet, but also illuminate the dominant role of recycled dolomite in modifying
476 mantle Mg isotopic composition.

477

478 **6.3. Relevance of the Neo-Tethyan seafloor subduction and the generation of**
479 **postcollisional ultrapotassic magmatism**

480 Sedimentary contribution to mantle heterogeneity can be identified through trace element
481 and isotopic geochemistry of mantle-derived magmas (White and Patchett, 1984). Based on
482 the discussion on Mg isotopic data and Hf/Sm variation in the UPVR, two geochemical
483 traverses were carried out with the aim of further investigating mantle refertilization processes
484 during the Tethyan seafloor subduction. As illustrated in Fig. 6, the UPVR samples in
485 southern Lhasa subterrane display mantle-like Hf/Sm and $\delta^{26}\text{Mg}$, but, in the central Lhasa
486 subterrane, the Hf/Sm and $\delta^{26}\text{Mg}$ of the UPVR appear to be more variable. Due to the scarcity
487 of UPVR outcropping in the northern Lhasa subterrane (Fig. 1a), it is untenable to ascribe the
488 observed spatial variations of Mg isotope and trace element indicators to the southward
489 subduction of Bangong-Nujiang Neo-Tethyan oceanic slab (cf. Zhu et al., 2013). We thus
490 interpret these northward geochemical variations as representing a clear pattern of mantle
491 refertilization during the northward subduction of the Indus-Yarlung Zangbo Neo-Tethyan
492 oceanic slab. Given that slab metamorphic dehydration would be gradually replaced by a
493 melting regime at greater depth (Schmidt and Poli, 2003), the decreasing $\delta^{26}\text{Mg}$ and Hf/Sm
494 from south to north may reflect the enhanced mantle carbonatite metasomatism with
495 Neo-Tethyan oceanic slab going deeper (Figs. 6 and 7a). This interpretation is in agreement
496 with the result of thermodynamic calculation (Connolly, 2005), which points out that
497 significant amount of marine carbonates may have survived from the decarbonation and
498 dissolution in sub-arc region and been transferred into deep earth.

499 In this regard, a two-stage petrogenetic model was proposed to link ultrapotassic
500 magmatism in the Lhasa terrane and mantle refertilization during the northward subduction of
501 Neo-Tethyan oceanic lithosphere. With the slab devolatilization processes gradually changed
502 from metamorphic dehydration to melting regime at greater depths, partial melts of
503 carbonate-bearing sediments stemmed from downgoing oceanic slab flux into the mantle
504 wedge, leaving clinopyroxene-rich mantle assemblage (i.e., wehrlite, Yang et al., 2012) with
505 isotopically light Mg (Fig. 7a). Under the background of continued underthrusting of Indian
506 continent, thermal perturbation induced by deep geodynamic processes (e.g. convective
507 thinning and/or delamination of the overthickened lithospheric mantle, roll-back and
508 break-off of Indian slab) would give rise to the partial melting of metasomatized mantle
509 sources and induce the Oligocene-Miocene ultrapotassic magmatism in southern Tibet (Fig.
510 7b). As evidenced by radiogenic Os isotopic compositions, entrained crustal xenoliths, and
511 zircon xenocrysts with pre-eruptive U–Pb ages, ultrapotassic magmas underwent different
512 extent of crustal contamination when they traveled through the overthickened Lhasa terrane
513 crust.

514

515 7. Conclusions

516 Systematic analyses of Os, Sr, and Mg isotopes on the Tibetan ultrapotassic rocks
517 elucidate the petrogenesis of potassium-rich mafic rocks and carbon recycling processes in
518 orogenic belts. The variably high $^{187}\text{Os}/^{188}\text{Os}$ in mantle-derived ultrapotassic rocks
519 demonstrate the widespread crustal contamination during magma ascent through the Lhasa
520 terrane crust. But high MgO contents permit Mg isotopes in ultrapotassic rocks essentially

521 unaffected by crustal contamination and enable Mg isotopic tracer to probe into the nature of
522 mantle sources. The isotopically light Mg in those low- $^{187}\text{Os}/^{188}\text{Os}$ ultrapotassic rocks is best
523 interpreted to reflect the subduction of carbonate-bearing sediments into mantle sources,
524 which are consistent with the negative Mg–Sr isotopic correlations and high CaO contents in
525 those HFSE-depleted primitive ultrapotassic samples. The positive co-variations between
526 $\delta^{26}\text{Mg}$ and Hf/Sm further highlight the potential of recycled dolomite to change mantle Mg
527 isotopic composition. The spatial variations in Hf/Sm and $\delta^{26}\text{Mg}$ correlate well with the
528 expected changes in devolatilization regime during the northward subduction of Neo-Tethyan
529 oceanic slab, suggesting that carbonatitic metasomatism **operating in mantle refertilization**
530 **beneath southern Tibet have laid the framework for generating** ultrapotassic rocks in
531 postcollisional stage.

532 **Acknowledgements**

533 We thank editor An Yin for handling this manuscript and M. S. Fantle for constructive
534 comments and suggestions. We are grateful to Jie Li, Cong Ding, Qing Meng, Shui-Jiong
535 Wang, and Sheng-Ao Liu for laboratory assistance and helpful discussion. This study was
536 financially supported by the National Key Project for Basic Research (project
537 2015CB452604), the Strategic Priority Research Program (B) of the Chinese Academy of
538 Sciences (project XDB03010301), the NSF of China (grants 41273044, 41225006, 41230209,
539 41130314), the NSF of U.S. (grants EAR-1111959, EAR-1340160, EAR-1056713,
540 EAR-0838227), and the Fundamental Research Funds for the Central Universities (grant
541 2652015280).
542

543 **References**

- 544 1. Avanzinelli, R., Lustrino, M., Mattei, M., Melluso, L., Conticelli, S., 2009. Potassic and
545 ultrapotassic magmatism in the circum-Tyrrhenian region: Significance of carbonated
546 pelitic vs. pelitic sediment recycling at destructive plate margins. *Lithos* 113, 213-227.
547 <http://dx.doi.org/10.1016/j.lithos.2009.03.029>
- 548 2. Blättler, C.L., Miller, N.R., Higgins, J.A., 2015. Mg and Ca isotope signatures of
549 authigenic dolomite in siliceous deep-sea sediments. *Earth Planet. Sci. Lett.* 419, 32-42.
550 <http://dx.doi.org/10.1016/j.epsl.2015.03.006>
- 551 3. Chung, S.-L., Chu, M.-F., Zhang, Y., Xie, Y., Lo, C.-H., Lee, T.-Y., Lan, C.-Y., Li, X.,
552 Zhang, Q., Wang, Y., 2005. Tibetan tectonic evolution inferred from spatial and
553 temporal variations in post-collisional magmatism. *Earth-Sci. Rev.* 68, 173-196.
554 <http://dx.doi.org/10.1016/j.earscirev.2004.05.001>
- 555 4. Coltorti, M., Bonadiman, C., Hinton, R., Siena, F., Upton, B., 1999. Carbonatite
556 metasomatism of the oceanic upper mantle: evidence from clinopyroxenes and glasses in
557 ultramafic xenoliths of Grande Comore, Indian Ocean. *J. Petrol.* 40, 133-165.
558 <http://dx.doi.org/10.1093/petroj/40.1.133>
- 559 5. Connolly, J.A.D., 2005. Computation of phase equilibria by linear programming: a tool
560 for geodynamic modeling and its application to subduction zone decarbonation. *Earth*
561 *Planet. Sci. Lett.* 236, 524-541. <http://dx.doi.org/10.1016/j.epsl.2005.04.033>
- 562 6. Conticelli, S., Avanzinelli, R., Ammannati, E., Casalini, M., 2015. The role of carbon
563 from recycled sediments in the origin of ultrapotassic igneous rocks in the Central
564 Mediterranean. *Lithos* 232, 174-196. <http://dx.doi.org/10.1016/j.lithos.2015.07.002>

- 565 7. Dasgupta, R., Hirschmann, M.M., 2010. The deep carbon cycle and melting in Earth's
566 interior. *Earth Planet. Sci. Lett.* 298, 1-13. <http://dx.doi.org/10.1016/j.epsl.2010.06.039>
- 567 8. Ducea, M.N., Saleeby, J., Morrison, J., Valencia, V.A., 2005. Subducted carbonates,
568 metasomatism of mantle wedges, and possible connections to diamond formation: an
569 example from California. *Am. Mineral.* 90, 864-870.
570 <http://dx.doi.org/10.2138/am.2005.1670>
- 571 9. Fantle, M.S., Higgins, J., 2014. The effects of diagenesis and dolomitization on Ca and
572 Mg isotopes in marine platform carbonates: Implications for the geochemical cycles of
573 Ca and Mg. *Geochim. Cosmochim. Acta* 142, 458-481.
574 <http://dx.doi.org/10.1016/j.gca.2014.07.025>
- 575 10. Galy, A., Yoffe, O., Janney, P.E., Williams, R.W., Cloquet, C., Alard, O., Halicz, L.,
576 Wadhwa, M., Hutcheon, I.D., Ramon, E., 2003. Magnesium isotope heterogeneity of the
577 isotopic standard SRM980 and new reference materials for magnesium-isotope-ratio
578 measurements. *J. Anal. At. Spectrom.* 18, 1352-1356.
579 <http://dx.doi.org/10.1039/B309273A>
- 580 11. Guo, Z., Wilson, M., Zhang, M., Cheng, Z., Zhang, L., 2013. Post-collisional, K-rich
581 mafic magmatism in south Tibet: constraints on Indian slab-to-wedge transport processes
582 and plateau uplift. *Contrib. Miner. Petrol.*, 1311-1340.
583 <http://dx.doi.org/10.1007/s00410-013-0860-y>
- 584 12. Ji, W.-Q., Wu, F.-Y., Chung, S.-L., Li, J.-X., Liu, C.-Z., 2009. Zircon U–Pb
585 geochronology and Hf isotopic constraints on petrogenesis of the Gangdese batholith,

- 586 southern Tibet. Chem. Geol. 262, 229-245.
587 <http://dx.doi.org/10.1016/j.chemgeo.2009.01.020>
- 588 13. Handley, H.K., Turner, S., Macpherson, C.G., Gertisser, R., Davidson, J.P., 2011. Hf–Nd
589 isotope and trace element constraints on subduction inputs at island arcs: Limitations of
590 Hf anomalies as sediment input indicators. Earth Planet. Sci. Lett. 304, 212-223.
591 <http://dx.doi.org/10.1016/j.epsl.2011.01.034>
- 592 14. Huang, S., Farkaš, J., Jacobsen, S.B., 2011. Stable calcium isotopic compositions of
593 Hawaiian shield lavas: evidence for recycling of ancient marine carbonates into the
594 mantle. Geochim. Cosmochim. Acta 75, 4987-4997.
595 <http://dx.doi.org/10.1016/j.gca.2011.06.010>
- 596 15. Huang, J., Li, S.-G., Xiao, Y., Ke, S., Li, W.-Y., Tian, Y., 2015. Origin of low $\delta^{26}\text{Mg}$
597 Cenozoic basalts from South China Block and their geodynamic implications. Geochim.
598 Cosmochim. Acta 164, 298-317. <http://dx.doi.org/10.1016/j.gca.2015.04.054>
- 599 16. Johnston, F.K.B., Turchyn, A.V., Edmonds, M., 2011. Decarbonation efficiency in
600 subduction zones: Implications for warm Cretaceous climates. Earth Planet. Sci. Lett.
601 303, 143-152. <http://dx.doi.org/10.1016/j.epsl.2010.12.049>
- 602 17. Kapp, P., DeCelles, P.G., Leier, A., Fabijanic, J.M., He, S., Pullen, A., Gehrels, G.E.,
603 Ding, L., 2007. The Gangdese retroarc thrust belt revealed. GSA Today 17, 4-9.
604 <http://dx.doi.org/10.1130/GSAT01707A.1>
- 605 18. Lee, H.Y., Chung, S.L., Lo, C.H., Ji, J., Lee, T.Y., Qian, Q., Zhang, Q., 2009. Eocene
606 Neotethyan slab breakoff in southern Tibet inferred from the Linzizong volcanic record.
607 Tectonophysics 477, 20-35. <http://dx.doi.org/10.1016/j.tecto.2009.02.031>

- 608 19. Li, J.-L., Klemd, R., Gao, J., Meyer, M., 2014. Compositional zoning in dolomite from
609 lawsonite-bearing eclogite (SW Tianshan, China): Evidence for prograde metamorphism
610 during subduction of oceanic crust. *Am. Mineral.* 99, 206-217.
611 <http://dx.doi.org/10.2138/am.2014.4507>
- 612 20. Li, W.-Y., Teng, F.-Z., Ke, S., Rudnick, R.L., Gao, S., Wu, F.-Y., Chappell, B., 2010.
613 Heterogeneous magnesium isotopic composition of the upper continental crust. *Geochim.*
614 *Cosmochim. Acta* 74, 6867-6884. <http://dx.doi.org/10.1016/j.gca.2010.08.030>
- 615 21. Liu, D., Zhao, Z., Zhu, D.-C., Niu, Y., DePaolo, D.J., Harrison, T.M., Mo, X., Dong, G.,
616 Zhou, S., Sun, C., Zhang, Z., Liu, J., 2014a. Postcollisional potassic and ultrapotassic
617 rocks in southern Tibet: Mantle and crustal origins in response to India-Asia collision
618 and convergence. *Geochim. Cosmochim. Acta* 143, 207-231.
619 <http://dx.doi.org/10.1016/j.gca.2014.03.031>
- 620 22. Liu, D., Zhao, Z., Zhu, D.-C., Niu, Y., Harrison, T.M., 2014b. Zircon xenocrysts in
621 Tibetan ultrapotassic magmas: Imaging the deep crust through time. *Geology* 42, 43-46.
622 <http://dx.doi.org/10.1130/G34902.1>
- 623 23. Liu, C.-Z., Wu, F.-Y., Chung, S.-L., Li, Q.-L., Sun, W.-D., Ji, W.-Q., 2014c. A ‘hidden’
624 ¹⁸O-enriched reservoir in the sub-arc mantle. *Sci. Rep.* 4.
625 <http://dx.doi.org/10.1038/srep04232>
- 626 24. Mazzullo, S.J., 2000. Organogenic Dolomitization in Peritidal to Deep-Sea Sediments. *J.*
627 *Sediment. Res.* 70, 10-23.
628 <http://dx.doi.org/10.1306/2DC408F9-0E47-11D7-8643000102C1865D>

- 629 25. Meisel, T., Walker, R.J., Irving, A.J., Lorand, J.P., 2001. Osmium isotopic compositions
630 of mantle xenoliths: a global perspective. *Geochim. Cosmochim. Acta* 65, 1311-1323.
631 [http://dx.doi.org/10.1016/S0016-7037\(00\)00566-4](http://dx.doi.org/10.1016/S0016-7037(00)00566-4)
- 632 26. Peccerillo, A., Federico, M., Barbieri, M., Brilli, M., Wu, T.-W., 2010. Interaction
633 between ultrapotassic magmas and carbonate rocks: evidence from geochemical and
634 isotopic (Sr, Nd, O) compositions of granular lithic clasts from the Alban Hills Volcano,
635 Central Italy. *Geochim. Cosmochim. Acta* 74, 2999-3022.
636 <http://dx.doi.org/10.1016/j.gca.2010.02.021>
- 637 27. Peucker-Ehrenbrink, B., Jahn, B.M., 2001. Rhenium-osmium isotope systematics and
638 platinum group element concentrations: Loess and the upper continental crust. *Geochem.*
639 *Geophys. Geosyst.* 2, 2001GC000172. <http://dx.doi.org/10.1029/2001GC000172>
- 640 28. Plank, T., Langmuir, C.H., 1998. The chemical composition of subducting sediment and
641 its consequences for the crust and mantle. *Chem. Geol.* 145, 325-394.
642 [http://dx.doi.org/10.1016/S0009-2541\(97\)00150-2](http://dx.doi.org/10.1016/S0009-2541(97)00150-2)
- 643 29. Ravizza, G., 1993. Variations of the $^{187}\text{Os}/^{186}\text{Os}$ ratio of seawater over the past 28 million
644 years as inferred from metalliferous carbonates. *Earth Planet. Sci. Lett.* 118, 335-348.
645 [http://dx.doi.org/10.1016/0012-821X\(93\)90177-B](http://dx.doi.org/10.1016/0012-821X(93)90177-B)
- 646 30. Rudnick, R.L., Gao, S., 2003. Composition of the continental crust. *Treatise Geochem.* 3,
647 1-64. <http://dx.doi.org/10.1016/B0-08-043751-6/03016-4>
- 648 31. Saal, A.E., Rudnick, R.L., Ravizza, G.E., Hart, S.R., 1998. Re–Os isotope evidence for
649 the composition, formation and age of the lower continental crust. *Nature* 393, 58-61.
650 <http://dx.doi.org/10.1038/29966>

- 651 32. Sapienza, G.T., Scambelluri, M., Braga, R., 2009. Dolomite-bearing orogenic garnet
652 peridotites witness fluid-mediated carbon recycling in a mantle wedge (Ulten Zone,
653 Eastern Alps, Italy). *Contrib. Miner. Petrol.* 158, 401-420.
654 <http://dx.doi.org/10.1007/s00410-009-0389-2>
- 655 33. Sánchez-Román, M., McKenzie, J.A., Wagener, A.L.R., Rivadeneyra, M.A.,
656 Vasconcelos, C., 2009. Presence of sulfate does not inhibit low-temperature dolomite
657 precipitation. *Earth Planet. Sci. Lett.* 285, 131-139.
658 <http://dx.doi.org/10.1016/j.epsl.2009.06.003>
- 659 34. Schaefer, B.F., Turner, S.P., Rogers, N.W., Hawkesworth, C.J., Williams, H.M., Pearson,
660 D.G., Nowell, G.M., 2000. Re–Os isotope characteristics of postorogenic lavas:
661 Implications for the nature of young lithospheric mantle and its contribution to basaltic
662 magmas. *Geology* 28, 563-566.
663 [http://dx.doi.org/10.1130/0091-7613\(2000\)28<563:RICOPL>2.0.CO;2](http://dx.doi.org/10.1130/0091-7613(2000)28<563:RICOPL>2.0.CO;2)
- 664 35. Schmidt, M.W., Poli, S., 2003. Generation of mobile components during subduction of
665 oceanic crust. *Treatise Geochem.* 3, 567-591.
666 <http://dx.doi.org/10.1016/B0-08-043751-6/03034-6>
- 667 36. Shirey, S.B., Walker, R.J., 1998. The Re–Os isotope system in cosmochemistry and
668 high-temperature geochemistry. *Annu. Rev. Earth Planet. Sci.* 26, 423-500.
669 <http://dx.doi.org/10.1146/annurev.earth.26.1.423>
- 670 37. Sun, S.S., McDonough, W.F., 1989. Chemical and isotopic systematics of oceanic basalts:
671 implications for mantle composition and processes. *Geol. Soc. London, Spec. Pub.* 42,
672 313-345. <http://dx.doi.org/10.1144/GSL.SP.1989.042.01.19>

- 673 38. Teng, F.-Z., Li, W.-Y., Ke, S., Marty, B., Dauphas, N., Huang, S., Wu, F.-Y., Pourmand,
674 A., 2010. Magnesium isotopic composition of the Earth and chondrites. *Geochim.*
675 *Cosmochim. Acta* 74, 4150-4166. <http://dx.doi.org/10.1016/j.gca.2010.04.019>
- 676 39. Teng, F.-Z., Yang, W., Rudnick, R.L., Hu, Y., 2013. Heterogeneous magnesium isotopic
677 composition of the lower continental crust: A xenolith perspective. *Geochem. Geophys.*
678 *Geosyst.* 14, 3844-3856. <http://dx.doi.org/10.1002/ggge.20238>
- 679 40. Thomsen, T.B., Schmidt, M.W., 2008. Melting of carbonated pelites at 2.5–5.0 GPa,
680 silicate-carbonatite liquid immiscibility, and potassium-carbon metasomatism of the
681 mantle. *Earth Planet. Sci. Lett.* 267, 17-31. <http://dx.doi.org/10.1016/j.epsl.2007.11.027>
- 682 41. Turner, S., Arnaud, N., Liu, J., Rogers, N., Hawkesworth, C., Harris, N., Kelley, S., Van
683 Calsteren, P., Deng, W., 1996. Post-collision, shoshonitic volcanism on the Tibetan
684 Plateau: Implications for convective thinning of the lithosphere and the source of ocean
685 island basalts. *J. Petrol.* 37, 45-71. <http://dx.doi.org/10.1093/petrology/37.1.45>
- 686 42. Wang, C., Hu, X., Sarti, M., Scott, R.W., Li, X., 2005. Upper Cretaceous oceanic red
687 beds in southern Tibet: a major change from anoxic to oxic, deep-sea environments.
688 *Cretaceous Res.* 26, 21-32. <http://dx.doi.org/10.1016/j.cretres.2004.11.010>
- 689 43. Wang, S.-J., Teng, F.-Z., Li, S.-G., 2014. Tracing carbonate-silicate interaction during
690 subduction using magnesium and oxygen isotopes. *Nat. Commun.* 5, 5328.
691 <http://dx.doi.org/10.1038/ncomms6328>
- 692 44. Wenzel, T., Baumgartner, L.P., Brüggemann, G.E., Konnikov, E.G., Kislov, E.V., 2002.
693 Partial melting and assimilation of dolomitic xenoliths by mafic magma: the

- 694 Ioko-Dovyren intrusion (North Baikal Region, Russia). *J. Petrol.* 43, 2049-2074.
695 <http://dx.doi.org/10.1093/petrology/43.11.2049>
- 696 45. White, W.M., Patchett, J., 1984. Hf–Nd–Sr isotopes and incompatible element
697 abundances in island arcs: implications for magma origins and crust-mantle evolution.
698 *Earth Planet. Sci. Lett.* 67, 167-185. [http://dx.doi.org/10.1016/0012-821X\(84\)90112-2](http://dx.doi.org/10.1016/0012-821X(84)90112-2)
- 699 46. Yang, W., Teng, F.-Z., Zhang, H.-F., Li, S.-G., 2012. Magnesium isotopic systematics of
700 continental basalts from the North China craton: Implications for tracing subducted
701 carbonate in the mantle. *Chem. Geol.* 328, 185-194.
702 <http://dx.doi.org/10.1016/j.chemgeo.2012.05.018>
- 703 47. Yin, A., Harrison, T.M., 2000. Geologic evolution of the Himalayan-Tibetan orogen.
704 *Annu. Rev. Earth Planet. Sci.* 28, 211-280.
705 <http://dx.doi.org/10.1146/annurev.earth.28.1.211>
- 706 48. Young, E.D., Galy, A., 2004. The isotope geochemistry and cosmochemistry of
707 magnesium. *Rev. Mineral. Geochem.* 55, 197-230.
708 <http://dx.doi.org/10.2138/gsrmg.55.1.197>
- 709 49. Zhao, Z., Mo, X., Dilek, Y., Niu, Y., DePaolo, D.J., Robinson, P., Zhu, D.-C., Sun, C.,
710 Dong, G., Zhou, S., 2009. Geochemical and Sr–Nd–Pb–O isotopic compositions of the
711 post-collisional ultrapotassic magmatism in SW Tibet: Petrogenesis and implications for
712 India intra-continental subduction beneath southern Tibet. *Lithos* 113, 190-212.
713 <http://dx.doi.org/10.1016/j.lithos.2009.02.004>

714 50. Zhu, D.-C., Zhao, Z.-D., Niu, Y., Dilek, Y., Hou, Z.-Q., Mo, X.-X., 2013. Origin and
715 pre-Cenozoic evolution of the Tibetan Plateau. *Gondwana Res.* 23, 1429-1454.
716 <http://dx.doi.org/10.1016/j.gr.2012.02.002>

717 **Figure captions**

718 **Fig. 1.** (a) Geological map of the Lhasa terrane, showing spatial distribution of the
719 Mesozoic-Cenozoic magmatism and sampling locations in this study. (b) Geographic
720 map of the Tibetan plateau. JSS = Jin Sha suture zone; BNS = Bangong-Nujiang suture
721 zone; SNMZ = Shiquan river-Nam Tso M \acute{e} lange zone; IYZS = Indus-Yarlung Zangbo
722 suture zone; ATF = Altyn Tagh fault; LMF = Luobadui-Milashan fault; KF =
723 Karakorum fault.

724
725 **Fig. 2.** (a) Total alkalis vs. SiO₂ diagram, with alkaline/sub-alkaline divide line indicated. (b)
726 Primitive mantle-normalized incompatible element patterns for the UPVR and the
727 entrained crustal xenoliths. Primitive mantle data are from [Sun and McDonough \(1989\)](#).
728 Dashed lines with different styles represent the incompatible element compositions of
729 calcite ([Ducea et al., 2005](#)) and dolomite ([Sapienza et al., 2009](#)) in mantle peridotites.
730 (c) Hf/Sm vs. Mg[#], and (d) Hf/Sm vs. CaO/Al₂O₃, showing that primitive ultrapotassic
731 rocks (high Mg[#]) have higher CaO/Al₂O₃ (i.e., high CaO content) and are more
732 depleted in HFSEs (i.e., Hf/Sm). Major and trace element data for the Tibetan UPVR
733 (cf. [Zhao et al., 2009](#); [Liu et al., 2014b](#)) and clinopyroxenes from mantle xenoliths (see
734 references in [Fig. S1](#)) are plotted for comparison.

735
736 **Fig. 3.** Os and Mg isotopic compositions of the Tibetan UPVR and entrained crustal xenoliths.
737 (a) ¹⁸⁷Os/¹⁸⁸Os vs. 1/Os. Os isotopic compositions for three presumed crustal
738 contaminants are given below: contaminant 1 (Os = 0.03 ppb, ¹⁸⁷Os/¹⁸⁸Os = 1.4),

739 contaminant 2 ($\text{Os} = 0.045$ ppb, $^{187}\text{Os}/^{188}\text{Os} = 0.85$), and contaminant 3 ($\text{Os} = 0.1$ ppb,
740 $^{187}\text{Os}/^{188}\text{Os} = 0.25$). R is the ratio between crustal assimilation rate and fractional
741 crystallization rate, and D_{Os} is the bulk partition coefficient for Os. The labeled
742 percentages along modeling curves donate the AFC increments. Os isotopic variation
743 predicted by magma mixing model is shown for comparison. Symbol sizes are greater
744 than the 10% analytic uncertainties. (b) $\delta^{25}\text{Mg}_{\text{DSM3}}$ vs. $\delta^{26}\text{Mg}_{\text{DSM3}}$, showing the Mg
745 isotopic data in this study is consistent with the mass-dependent fractionation trend.
746 Error bars of Mg isotopic ratios represent two standard deviations, and β represents the
747 exponent in the mass-dependent fractionation law (Young and Galy, 2004). (c)
748 $\delta^{26}\text{Mg}_{\text{DSM3}}$ vs. $^{187}\text{Os}/^{188}\text{Os}$, showing co-variation trends defined by Os and Mg isotopes
749 of the UPVR samples and gabbroic xenolith. Mantle carbonatite metasomatism is
750 modeled in terms of binary mixing between carbonate melts (dolomite and calcite) and
751 mantle lherzolite. Os and Mg isotopic compositions of end-members are given in Table
752 S7. Mixing hyperbolas are marked in 10% increments. Based on Os isotopic variation
753 in Fig. 3a, $R = 0.8$ and $D_{\text{Os}} = 10$ are used in modeling AFC processes. Assuming
754 cumulates of phlogopite + clinopyroxene + olivine, bulk partition coefficient for Mg
755 (D_{Mg}) is set at 4 ± 2 . The uncertainty in D_{Mg} is indicated by color-shaded area with
756 dashed lines for each solid AFC modeling curve. Circles on the AFC modeling curves
757 indicate 2% AFC increments. Os and Mg isotopic ranges of normal mantle reservoir
758 (Meisel et al., 2001; Teng et al., 2010) are shown for comparison.

759

760 **Fig. 4.** Diagrams of (a) CaO/SiO₂ vs. MgO and (b) δ¹⁸O_{V-SMOW} vs. SiO₂, showing isotopic and
761 element variations of the Tibetan UPVR and the Italian ultrapotassic rocks that
762 underwent contamination of the Apennine carbonates (cf. [Peccerillo et al., 2010](#)).
763 Oxygen isotopic data of the Tibetan UPVR are from [Zhao et al. \(2009\)](#) and [Liu et al.](#)
764 [\(2014\)](#) and references therein. Note that CaO contents of the Tibetan UPVR are
765 apparently lower than that of the Italian ultrapotassic rocks that were contaminated by
766 dolostone and limestone during magmatic evolution. The positive δ¹⁸O_{V-SMOW}-SiO₂
767 correlation defined by the Tibetan UPVR contrasts with the negative trends found in
768 the Italian ultrapotassic rocks, precluding contamination of sedimentary carbonates as a
769 controlling process in generating isotopic signatures of the Tibetan UPVR.

770
771 **Fig. 5.** Isotopic fingerprints of mantle carbonatite metasomatism recorded in the Tibetan
772 ultrapotassic rocks. (a) δ²⁶Mg_{DSM3} vs. ⁸⁷Sr/⁸⁶Sr plot for less-contaminated ultrapotassic
773 rocks with ¹⁸⁷Os/¹⁸⁸Os lower than 0.3 (i.e. UPVR samples in trend B, [Fig. 3c](#)), showing
774 that both crustal contamination and mantle metasomatism have contributed to isotopic
775 variations in the Tibetan UPVR. Carbonatitic metasomatism is modeled in terms of
776 binary mixing between carbonates (Sr = 800 ppm, ⁸⁷Sr/⁸⁶Sr = 0.709) and mantle
777 lherzolite (Sr = 21.1 ppm, ⁸⁷Sr/⁸⁶Sr = 0.703) ([Table S7](#)). AFC processes are modeled to
778 show ⁸⁷Sr/⁸⁶Sr increments during crustal contamination. Varying ⁸⁷Sr/⁸⁶Sr and δ²⁶Mg
779 are assumed for ultrapotassic magmas (Sr = 1200 ppm). AFC modeling curves are
780 marked in 5% increments, where R is 0.8 and D_{Mg} is 4 ± 2. Bulk partition coefficients
781 for Sr (D_{Sr}) is set at 0.7. Crustal contaminant is assumed to have radiogenic Sr isotopic

782 composition ($\text{Sr} = 320 \text{ ppm}$, $^{87}\text{Sr}/^{86}\text{Sr} = 0.756$; Liu et al., 2014a), and its Mg isotopic
783 composition is similar to that of upper continental crust (Table S7). Shadowed area in
784 Fig. 5a indicates crustal contamination occurred at relatively low level ($\text{AFC} < 10\%$).
785 Note that the variations in $\delta^{26}\text{Mg}$ are very limited when crustal contamination occurred
786 at low level. (b) $\delta^{26}\text{Mg}_{\text{DSM3}}$ vs. Hf/Sm diagram, showing the dominant role of
787 dolomites in changing mantle Mg isotopic composition. Given the intrinsic Mg
788 isotopic variations in marine dolomites (Blättler et al., 2015) and their major and trace
789 element changes during prograde metamorphism (Li et al., 2014), subducted dolomites,
790 with ranges of $\delta^{26}\text{Mg}$, Hf/Sm, and MgO, are used for modeling carbonatitic
791 metasomatism (see Table S7 for details). The binary mixing curves of mantle
792 carbonatite metasomatism are marked in 10% increments and labeled with
793 corresponding Mg/Ca ratio of recycled carbonates. The Hf/Sm and $\delta^{26}\text{Mg}$ data for
794 oceanic basalts (MORB and OIB, Sun and McDonough, 1989; Teng et al., 2010),
795 kamafugites from Qinling orogenic belt (our unpublished data), the Cretaceous basalts
796 from north China craton (Yang et al., 2012), and the Cenozoic basalts from south
797 China (Huang et al., 2015) are plotted for comparison.

798
799 **Fig. 6.** Geochemical traverses (see Fig. 1a) showing spatial variation of Mg isotope and
800 Hf/Sm ratio in ultrapotassic rocks. For comparison, two traverses have been corrected
801 to positions relative to the LMF and SNMZ in the Lhasa terrane. Pink arrows indicate
802 the enhancing role of mantle carbonatite metasomatism from south to north. The
803 Hf/Sm range of arc magmas (White and Patchett, 1984) is shown for comparison.

804

805 **Fig. 7.** A two-stage geodynamic model consists of (a) mantle carbonatite metasomatism
806 during the northward subduction of the Neo-Tethyan seafloor, and (b) generation of the
807 Oligocene-Miocene ultrapotassic magmatism in a tectonic setting of continental
808 convergence. The devolatilization pattern during the northward subduction of the
809 Neo-Tethyan oceanic lithosphere (> 65 Ma) changed from metamorphic dehydration to
810 a melting regime, which may correspond to more dolomites transported to the
811 subcontinental lithospheric mantle. CC denotes continental crust.

812 **Table captions**

813 **Table 1 Os–Sr–Mg isotopic compositions of Tibetan ultrapotassic rocks and crustal**
814 **xenoliths**

815 - * Elemental and Sr isotopic compositions of these samples have been reported in [Zhao et al.](#)
816 [\(2009\)](#). Their Os and Mg isotopes were determined in the Miami University and the
817 University of Arkansas, respectively.

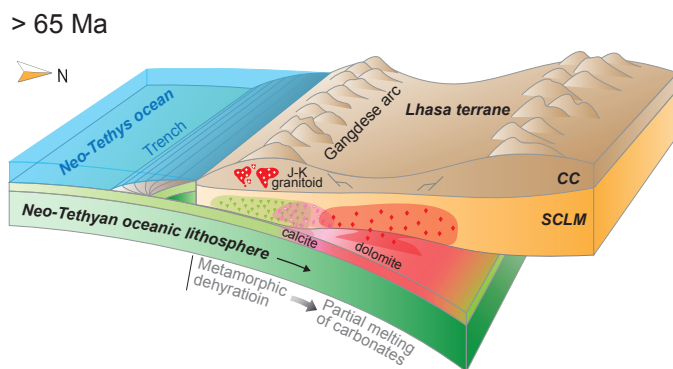
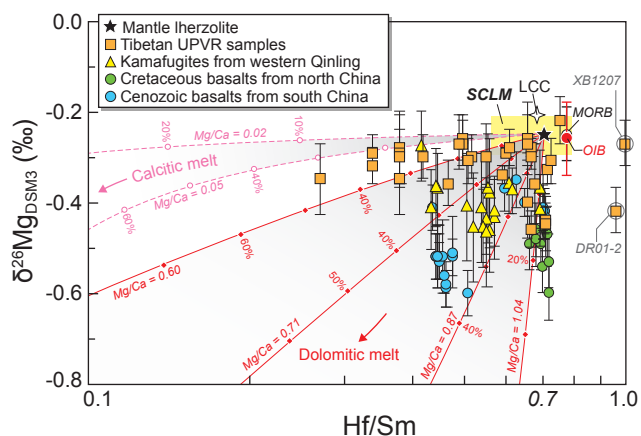
818 - *Os-Rep* = replicate Os data for separate digestions of different sample aliquots. *Mg-Rep* =
819 repeat sample dissolution, column chemistry and instrumental analysis.

820 - 2σ = 2 times the standard deviation of the population of four repeat measurements of a
821 sample solution.

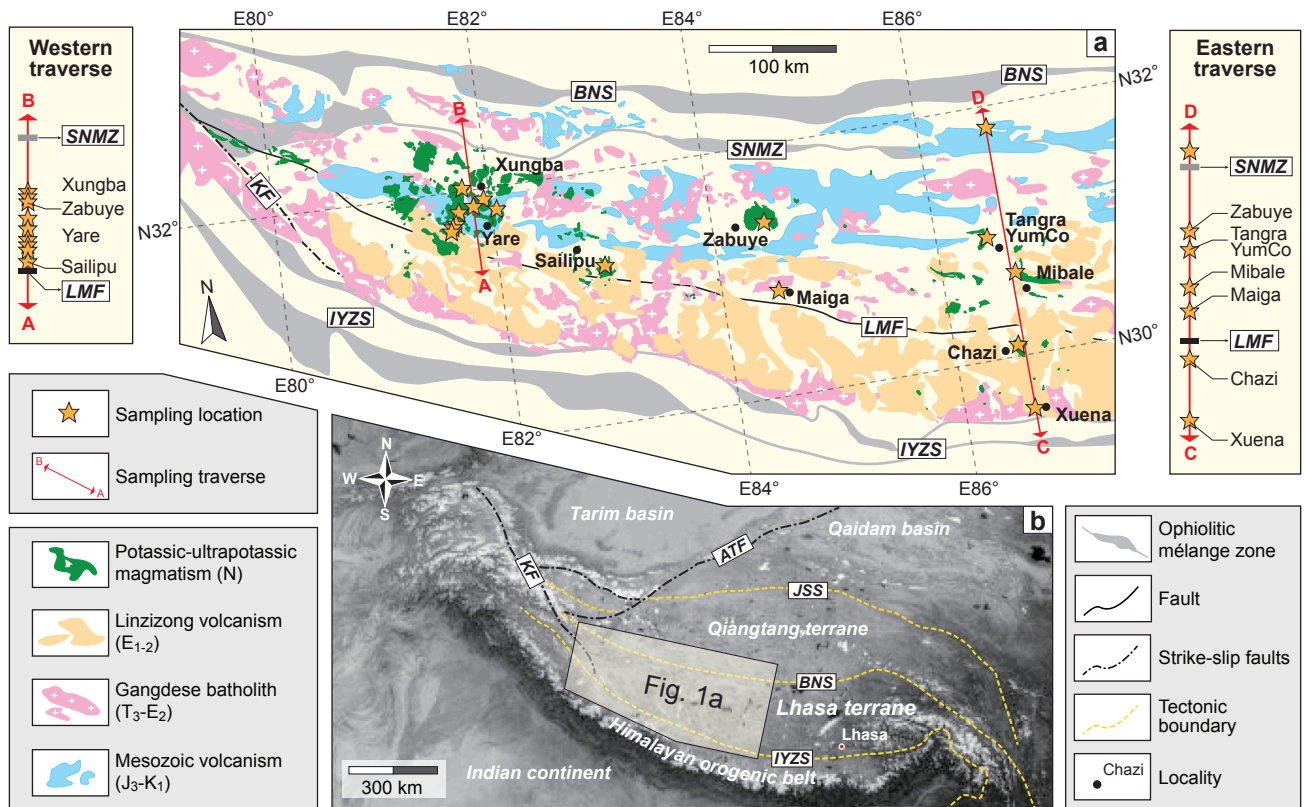
822 - XB-YR, Xungba and Yare area; BtA, basaltic trachyandesite; Te, tephrite; TeP,
823 tephriphonolite; Tr, trachyte; TrA, trachyandesite.

824 - Samples XB1257 and XB1258 are the host ultrapotassic rocks for gabbroic (XB1260) and
825 granitic (XB1261) xenoliths, respectively.

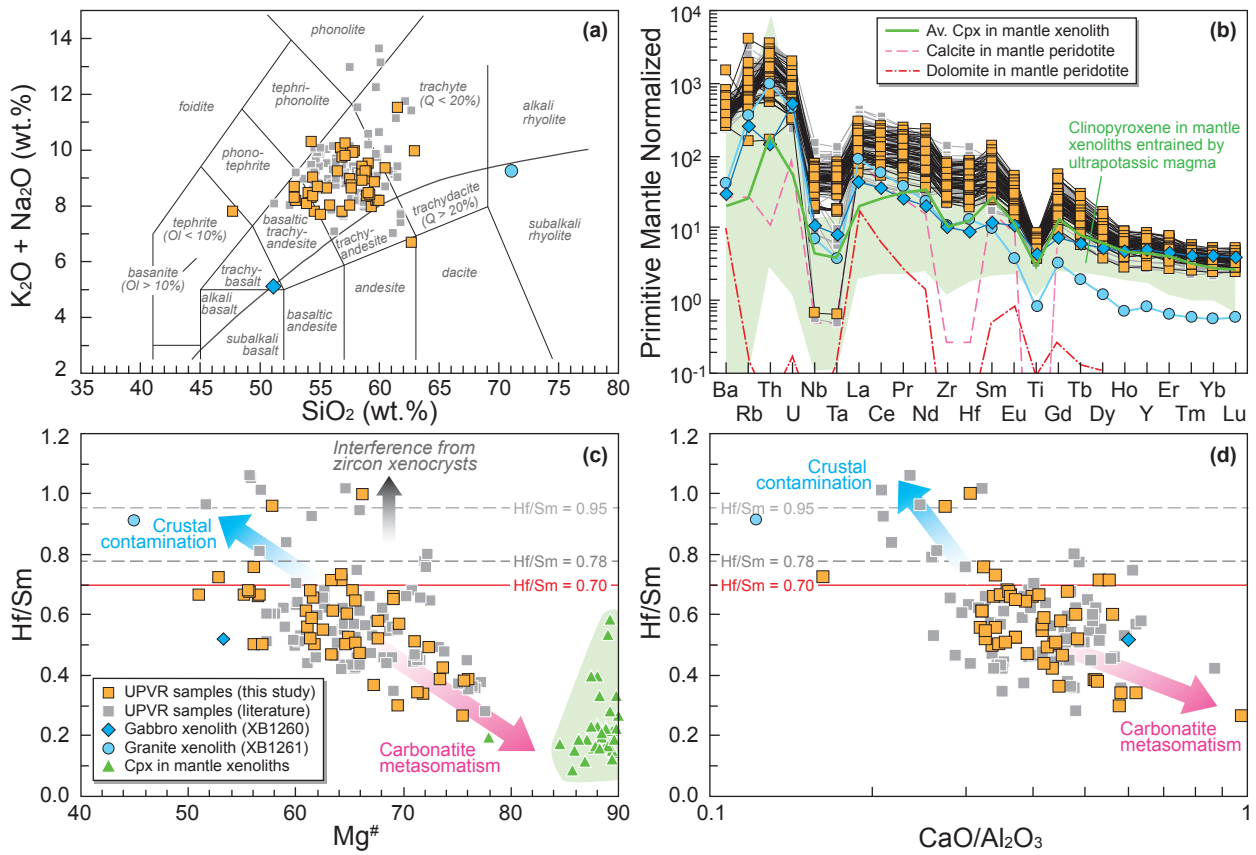
Graphical abstract



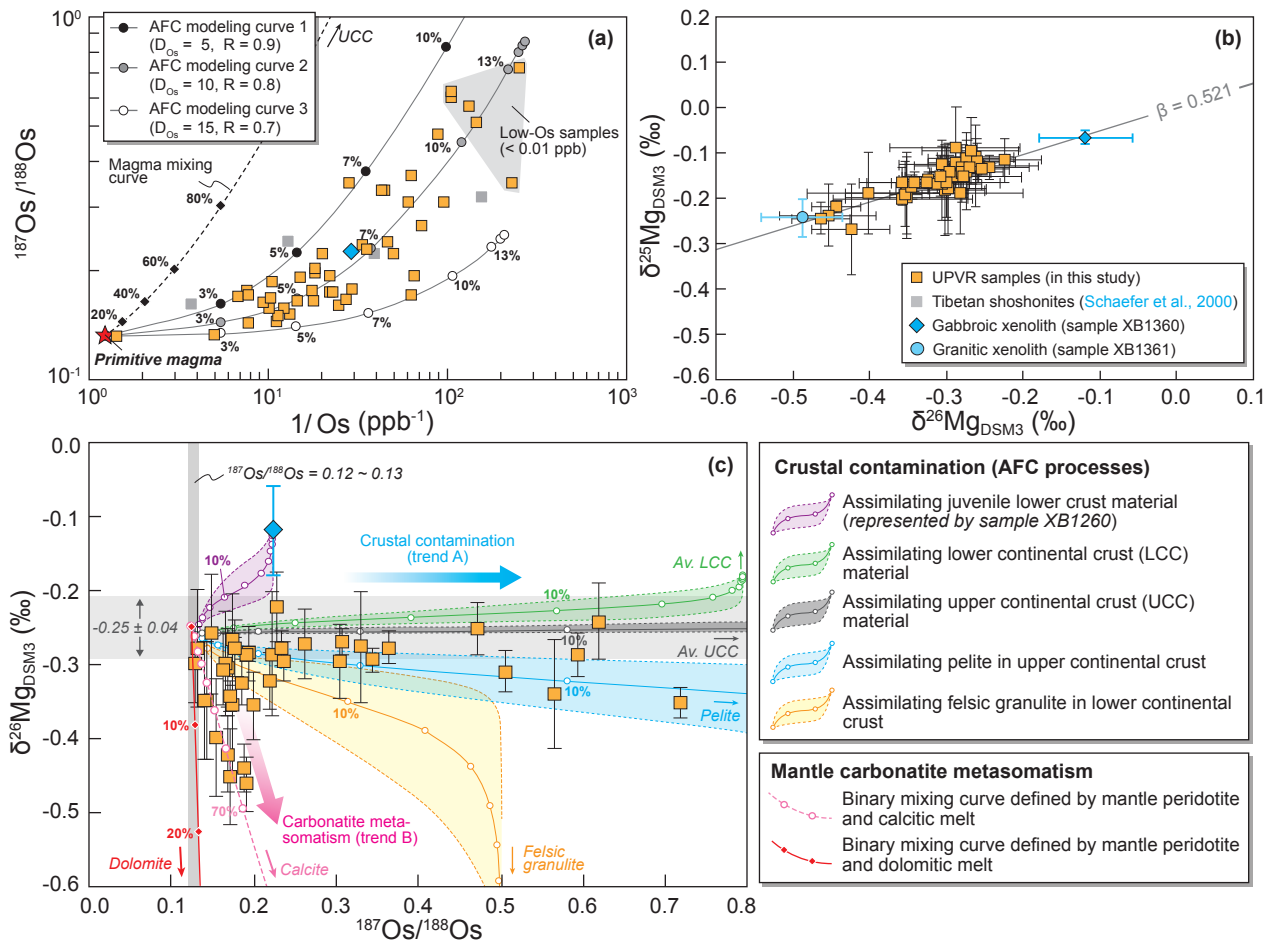
Liu et al. **Fig. 1** W171 mm - H106 mm (2-column fitting image)



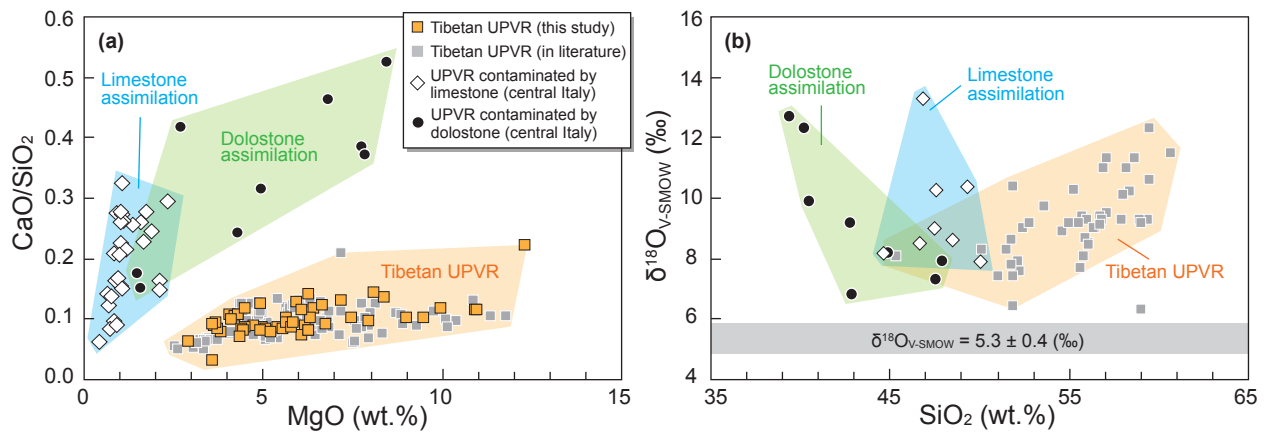
Liu et al. **Fig. 2** W167 mm - H112 mm (2-column fitting image)



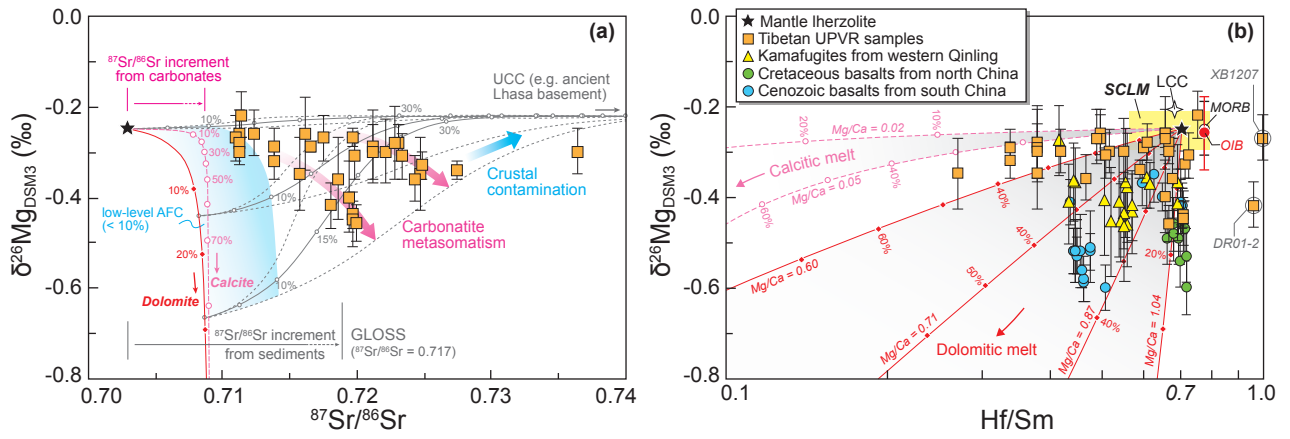
Liu et al. **Fig. 3** W166 mm - H125 mm (2-column fitting image)



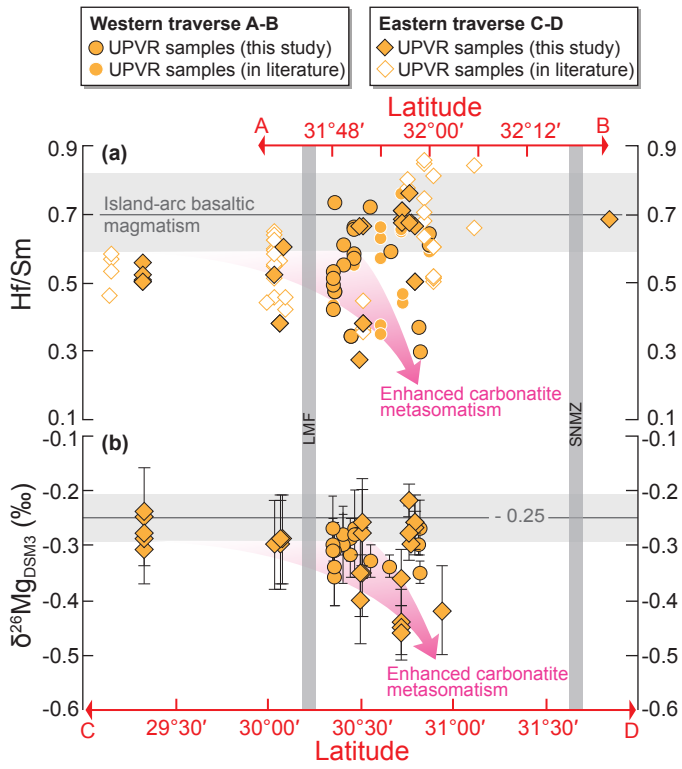
Liu et al. **Fig. 4** W166 mm - H156 mm (2-column fitting image)



Liu et al. **Fig. 5** W165 mm - H58 mm (two-column fitting image)



Liu et al. **Fig. 6** W89 mm - H101 mm (single-column fitting image)



Liu et al. Fig. 7 W89 mm - H105 mm (single-column fitting image)

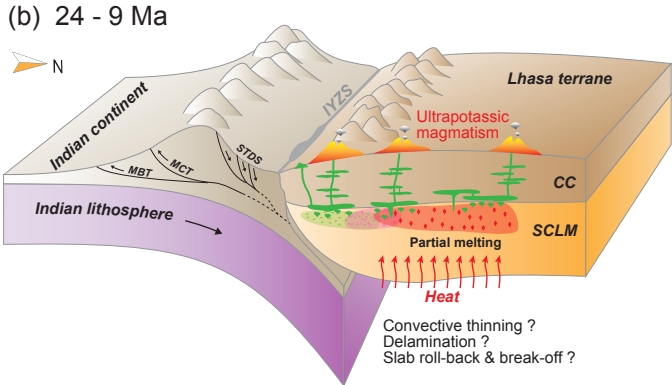
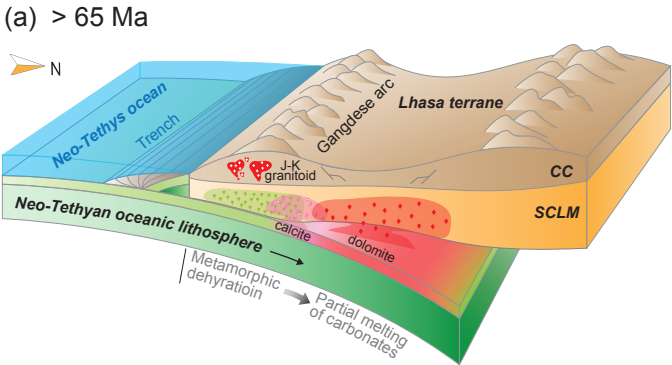


Table 1 Os–Sr–Mg isotopic compositions of Tibetan ultrapotassic rocks and crustal xenoliths

Sample No.	Locality	Lith.	Mg [#]	Hf/Sm	Re (ppb)	Os (ppb)	¹⁸⁷ Re/ ¹⁸⁸ Os	¹⁸⁷ Os/ ¹⁸⁸ Os		⁸⁷ Sr/ ⁸⁶ Sr		$\delta^{25}\text{Mg}$ (‰)	$\pm 2\sigma$	$\delta^{26}\text{Mg}$ (‰)	$\pm 2\sigma$
								Ratio	$\pm 2\sigma$	Ratio	$\pm 2\sigma$				
Ultrapotassic volcanic rocks (UPVR)															
CQ01*	Maiga	BtA	76.0	0.38	0.047	0.199	1.13	0.1324	0.0001	0.722810		-0.19	0.09	-0.28	0.08
CQ02*	Maiga	TrA	56.5	0.66	0.051	0.076	3.23	0.1509	0.0001	0.716194		-0.13	0.09	-0.26	0.08
CQ03*	Maiga	BtA	73.5	0.38	0.016	0.089	0.87	0.1441	0.0001	0.724697		-0.19	0.09	-0.35	0.08
D9103*	Maiga	TrA	61.6	0.66	0.044	0.081	2.63	0.1572	0.0002	0.719414		-0.19	0.09	-0.40	0.08
GGP-7*	Maiga	Te	75.6	0.27	0.070	0.128	2.65	0.1423	0.0001	0.715817		-0.20	0.09	-0.35	0.08
<i>Os-Rep</i>	Maiga	Te			0.093	0.087	5.18	0.1492	0.0001						
XR01-3*	Chazi	BtA	75.7	0.38	0.073	0.020	17.9	0.2226	0.0003	0.721161		-0.09	0.09	-0.29	0.08
<i>Mg-Rep</i>	Chazi	BtA										-0.13	0.05	-0.30	0.06
XR02-1*	Chazi	TeP	67.7	0.52	0.014	0.698	0.09	0.1315	0.0001	0.736451		-0.18	0.10	-0.30	0.05
DR1102	Chazi	TrA	64.9	0.60	0.004	0.015	1.14	0.1924	0.0008	0.716657	0.000011	-0.15	0.03	-0.29	0.01
DR01-2*	Mibale	Tr	57.9	0.96	0.056	0.016	17.2	0.1710	0.0002	0.718043		-0.27	0.10	-0.42	0.05
Z8030-18*	Tangra	TrA	61.4	0.68	0.055	0.069	3.87	0.1647	0.0001	0.719632					
<i>Os-Rep</i>	YumCo	TrA			0.058	0.097	2.90	0.1567	0.0001						
DR1103	Mibale	TrA	64.3	0.71	0.075	0.066	5.58	0.1904	0.0003	0.719745	0.000012	-0.22	0.01	-0.44	0.03
DR1107	Mibale	TrA	65.3	0.68	0.088	0.056	7.63	0.1746	0.0004	0.718702	0.000013	-0.20	0.01	-0.36	0.09
DR1113	Mibale	TrA	63.3	0.71	0.019	0.045	2.06	0.1734	0.0005	0.719773	0.000012	-0.24	0.07	-0.45	0.06
DR1114	Mibale	TrA	51.0	0.67	0.022	0.045	2.36	0.1934	0.0005	0.719961	0.000011	-0.25	0.04	-0.46	0.04
ZB1*	Zabuye	TrA	56.1	0.50						0.711352		-0.11	0.04	-0.26	0.05
ZB4*	Zabuye	TrA	57.0	0.50						0.711075		-0.11	0.04	-0.27	0.05
ZB12*	Zabuye	TrA	56.6	0.66						0.712408		-0.12	0.04	-0.26	0.05
ZB1102	Zabuye	TrA	55.3	0.67	0.132	0.030	21.6	0.2341	0.0005	0.711252	0.000011	-0.13	0.02	-0.28	0.02
ZB1108	Zabuye	TrA	56.1	0.76	0.121	0.028	21.2	0.2288	0.0009	0.711373	0.000011	-0.12	0.05	-0.22	0.05
ZB1112	Zabuye	TrA	55.7	0.67	0.105	0.021	24.2	0.2387	0.0005	0.711241	0.000010	-0.18	0.07	-0.30	0.03
SL0621*	Sailipu	TrA	72.4	0.49	0.094	0.130	3.51	0.1747	0.0001			-0.10	0.07	-0.27	0.06
<i>Os-Rep</i>	Sailipu	TrA			0.090	0.148	3.51	0.1684	0.0001						
SL0626*	Sailipu	TrA	64.9	0.53	0.025	0.105	1.15	0.1624	0.0002						
SL0630*	Sailipu	TrA	73.7	0.42	0.026	0.010	12.1	0.3067	0.0004			-0.18	0.10	-0.30	0.05
SLP1101	Sailipu	TrA	71.1	0.51	0.065	0.128	2.48	0.1707	0.0003	0.719810	0.000013	-0.17	0.08	-0.31	0.05
XN1201	Xuena	TrA	61.8	0.50	0.024	0.009	13.0	0.5956	0.0016	0.711178	0.000012	-0.15	0.03	-0.29	0.03
XN1203	Xuena	TrA	61.4	0.52	0.031	0.009	16.6	0.6191	0.0023	0.711569	0.000010	-0.13	0.03	-0.24	0.05
XN1206	Xuena	TrA	64.7	0.50	0.005	0.016	1.72	0.3653	0.0012	0.711474	0.000012	-0.15	0.06	-0.28	0.02
XN1207	Xuena	TrA	61.1	0.56	0.016	0.011	7.29	0.4717	0.0012	0.710747	0.000011	-0.14	0.01	-0.25	0.04
XN1208	Xuena	TrA	65.6	0.51	0.025	0.007	18.6	0.5081	0.0022	0.713008	0.000012	-0.17	0.02	-0.31	0.03
10XB11	XB-YR	TrA	65.6	0.64	0.006	0.040	0.71	0.1596	0.0004						
10XB15	XB-YR	Tr	61.0	0.61	0.013	0.096	0.64	0.1677	0.0003						
10YR02	XB-YR	TrA	61.7	0.58	0.416	0.035	58.8	0.3461	0.0009						
10YR06	XB-YR	TrA	69.7	0.57	0.044	0.022	9.66	0.3299	0.0009						
XB1207	XB-YR	TrA	66.2	1.00	0.102	0.014	35.7	0.2644	0.0009	0.717597	0.000012	-0.14	0.09	-0.27	0.05
XB1210	XB-YR	TrA	69.5	0.30	0.083	0.004	109.6	0.7197	0.0034	0.720108	0.000010	-0.19	0.07	-0.35	0.02
XB1214	XB-YR	TrA	67.3	0.36	0.052	0.004	58.6	0.3466	0.0015	0.718906	0.000012	-0.14	0.01	-0.30	0.02
XB1230	XB-YR	TrA	61.5	0.59	0.037	0.043	4.19	0.1736	0.0004	0.727526	0.000012	-0.18	0.03	-0.34	0.02
XB1232	XB-YR	Tr	52.8	0.72	0.033	0.095	1.68	0.1863	0.0004	0.724916	0.000013	-0.17	0.00	-0.33	0.03
XB1233	XB-YR	TrA	62.5	0.55	0.055	0.037	7.25	0.1661	0.0004	0.722197	0.000011	-0.17	0.08	-0.30	0.07
XB1234	XB-YR	TrA	63.4	0.61	0.057	0.034	8.18	0.1773	0.0006	0.723080	0.000011	-0.14	0.01	-0.28	0.04
XB1237	XB-YR	TrA	64.3	0.73	0.096	0.055	8.41	0.1639	0.0004	0.723372	0.000011	-0.15	0.04	-0.31	0.05
XB1241	XB-YR	TrA	63.4	0.47	0.069	0.054	6.18	0.2024	0.0004	0.724377	0.000011	-0.17	0.03	-0.36	0.05
XB1242	XB-YR	TrA	65.9	0.47	0.065	0.008	43.9	0.5659	0.0026	0.725390	0.000012	-0.17	0.02	-0.34	0.07
XB1253	XB-YR	TrA	69.1	0.66	0.039	0.016	11.8	0.3088	0.0007	0.719685	0.000011	-0.13	0.05	-0.27	0.02
XB1254	XB-YR	TrA	69.1	0.65	0.119	0.023	25.5	0.3322	0.0006	0.719629	0.000011	-0.15	0.03	-0.28	0.08
XB1257	XB-YR	TrA	71.9	0.34	0.019	0.050	1.89	0.2218	0.0006	0.713924	0.000010	-0.16	0.02	-0.32	0.04
XB1258	XB-YR	BtA	71.4	0.34	0.008	0.054	0.69	0.1953	0.0005	0.713877	0.000011	-0.12	0.03	-0.29	0.04
Crustal xenoliths															
XB1260	XB-YR	Gabbro	55.8	0.52	0.132	0.034	18.79	0.2249	0.0007	0.709763	0.000013	-0.07	0.01	-0.12	0.06
XB1261	XB-YR	Granite	47.6	0.91						0.713443	0.000011	-0.24	0.04	-0.49	0.05

- * Elemental and Sr isotopic compositions of these samples have been reported in [Zhao et al. \(2009\)](#). Their Os and Mg isotopes were determined in the Miami University and the University of Arkansas, respectively.

- *Os-Rep* = replicate Os data for separate digestions of different sample aliquots. *Mg-Rep* = repeat sample dissolution, column chemistry and instrumental analysis.

- 2σ = 2 times the standard deviation of the population of four repeat measurements of a sample solution.

- XB-YR, Xungba and Yare area; BtA, basaltic trachyandesite; Te, tephrite; TeP, tephriphonolite; Tr, trachyte; TrA, trachyandesite.

- Samples XB1257 and XB1258 are the host ultrapotassic rocks for gabbroic (XB1260) and granitic (XB1261) xenoliths, respectively.